Formation of the double stratopause and elevated stratopause associated with the major stratospheric sudden warming in 2018/19

Haruka Okui[1], Kaoru Sato[1], Dai Koshin[1], and Shingo Watanabe[2]

[1]Department of Earth and Planetary Science, Graduate School of Science, The University of Tokyo, Tokyo, Japan

[2]Japan Agency for Marine–Earth Science and Technology, Yokohama, Japan

Corresponding author: Haruka Okui (okui@eps.s.u-tokyo.ac.jp)

Key Points:

- A hindcast of the 2018/19 stratospheric sudden warming was performed using a gravity-wave permitting high-top general circulation model.
- Planetary waves excited by gravity wave forcing contribute to the formation of a double stratopause, two temperature peaks in the vertical.
- Both planetary wave and gravity wave forcing contribute to the formation of the elevated stratopause.

Abstract

After several recent stratospheric sudden warming (SSW) events, the stratopause disappeared and reformed at a higher altitude, forming an elevated stratopause (ES). The relative roles of atmospheric waves in the mechanism of ES formation are still not fully understood. We performed a hindcast of the 2018/19 SSW event using a gravity-wave (GW) permitting general circulation model containing the mesosphere and lower thermosphere (MLT), and analyzed dynamical phenomena throughout the entire middle atmosphere. An ES formed after the major warming on 1 January 2019. There was a marked temperature maximum in the polar upper mesosphere around 28 December 2018 prior to the disappearance of the descending stratopause associated with the SSW. This temperature structure with two maxima in the vertical is referred to as a double stratopause (DS). We showed that adiabatic heating from the residual circulation driven by GW forcing (GWF) causes barotropic and/or baroclinic instability before DS formation, causing in situ generation of planetary waves (PWs). These PWs propagate into the MLT and exert negative forcing, which contributes to DS formation. Both negative GWF and PWF above the recovered eastward jet play crucial roles in ES formation. The altitude of the recovered eastward jet, which regulates GWF and PWF height, is likely affected by the DS structure. Simple vertical propagation from the lower atmosphere is insufficient to explain the presence of the GWs observed in this event.

1 Introduction

Dynamical events called stratospheric sudden warmings (SSWs) greatly alter the thermal and dynamical conditions in the winter stratosphere. They are results of the interaction between upward propagating planetary waves (PWs) and zonal mean fields (Matsuno, 1971). The occurrence of an SSW is indicated by a rapid increase in the temperature and the weakening or reversal of the eastward jet in the winter polar stratosphere. The World Meteorological Organization defines a positive poleward gradient of the zonal mean temperature from 60° latitude to the pole accompanied by a reversal of the zonal-mean zonal wind at 60° latitude at or below 10hPa as a major SSW; a minor SSW only satisfies the first condition. On the basis of the shape of the polar vortex, SSWs can also be classified into displacement and splitting events (e.g., Charlton and Polvani, 2007).

An SSW can be recognized as a descending stratopause. After the onset of the past several SSWs, specifically the 2006, 2009, 2013 and 2019 events, the stratopause, which has descended to a lower altitude, became indistinct and then reformed at an altitude above its climatological height. This phenomenon is called an elevated stratopause (ES) (e.g., Manney et al., 2008, 2009; Siskind et al., 2010). Several previous observational and numerical studies showed that gravity wave (GW) forcing (GWF) induces the formation and descent of the ES (e.g., Tomikawa et al., 2012; Siskind et al., 2007, 2010; Thurairajah et al., 2014). Using a

GW-permitting general circulation model (GCM) of the KANTO project (Watanabe et al., 2008), Tomikawa et al. (2012) analyzed a simulated major SSW event. They showed that positive PW forcing (PWF) leads to the quick recovery of the polar eastward jet after the major SSW, and negative GWF above the recovered jet contributes to the formation of the ES. Thurairajah et al. (2014) provided observational evidence of the enhancement of GW activity after SSWs using global high-latitude temperature measurements from the Solar Occultation for Ice Experiment (SOFIE).

The crucial role of PWs in the initial phase of ES formation has also been suggested (e.g., Limpasuvan et al., 2012, 2016; Chandran et al., 2011, 2013). Limpasuvan et al. (2016) conducted a composite analysis of 13 SSW-ES events identified in the runs of the Whole Atmosphere Community Climate Model, Version 4 with specified dynamics (SD-WACCM) for 1990–2013. They showed that downward flow induced by negative PWF in the polar mesosphere and lower thermosphere (MLT) is responsible for ES formation. Several observational studies have pointed out that the amplitudes of PWs with zonal wavenumber s= 1–2 increase in the MLT when an ES event occurs (e.g., Stray et al., 2015). However, it has also been indicated that PWF in the MLT is not necessarily strong during ES formation. Chandran et al. (2013) showed that in a few events in model simulations, the entire process of ES formation appears to be driven by GWF despite the climatological importance of PWF. The relative contributions of GWs and PWs to ES formation remain to be elucidated.

The ES phenomenon, which is accompanied by downwelling in the MLT, strongly influences downward material transport and thus the coupling between the MLT and the stratosphere (e.g., Randall et al., 2009). For example, NOx (=NO+NO_2) produced by energetic particle precipitation (EPP) in the MLT is transported into the stratosphere, especially during ES events that occur in early winter. In the region under the influence of the polar night, NOx is long-lived and causes ozone depletion in the stratosphere (e.g., Holt et al., 2013; Randall et al., 2009). This effect, referred to as the EPP indirect effect, is very important in chemistry–climate models because it affects the dynamics of the stratosphere (e.g., Siskind et al., 2015). Smith et al. (2018) also pointed out that the enhanced downward flow associated with ES events results in a downward shift in the maximum altitude of ozone concentrations.

However, most high-top models tend to underestimate downward material transport in the MLT during ES events (e.g., Randall et al., 2015; Orsolini et al., 2017). In addition, ES height is generally lower in the model than in observation data. These model biases are the results of the underestimation (overestimation) of downward motion in the upper (lower) mesosphere (e.g., Funke et al., 2017). Meraner et al. (2016) showed that the intensity of the parameterized nonorographic GW sources affects the height of GWF in the MLT. The modulation of the height of GWF can affect the amount of downward material transport.

They reported that weaker GW sources in the parameterization yield a better agreement of simulations with observations.

To elucidate the relative importance of PWs and GWs in dynamical phenomena in the middle atmosphere, the in-situ generation of waves should be taken into consideration. Several studies showed that strong Rossby wave (RW) breaking causes the barotropic (BT) and/or baroclinic (BC) instability, which excites RWs (e.g., Baldwin and Holton, 1988; Hitchman and Huesmann, 2007; Greer et al., 2013). Smith (1996, 2003) suggested that momentum deposit by the GWs that have been filtered by planetary-scale wind structures in the stratosphere lead to in situ generation of PWs in the middle and upper mesosphere. On the basis of a case study of a boreal winter using the KANTO model, Sato and Nomoto (2015) suggested the importance of the interplay of GWs and PWs in the middle atmosphere. They provided evidence of in-situ PW generation due to the BT/BC instability resulting from the generation of a potential vorticity (PV) maximum attributed to GWF. Positive and negative PWFs associated with the PW generation act to eliminate this PV maximum. Using the KANTO model, Watanabe et al. (2009) showed that in the Antarctic winter mesosphere eastward 4-day waves are generated by the BT/BC instability which develops in the large-scale mean flow strongly distorted by GWF. Sato et al. (2018) and Yasui et al. (2018) showed that the BT/BC instability and shear instability caused by GWs originating from the lower atmosphere generate RWs and GWs in the mesosphere, respectively. Recently, Vadas and Becker (2018) suggested that momentum deposit associated with the breaking of orographic GWs generates secondary GWs in the stratosphere and lower mesosphere in the southern polar region in winter.

Most high-top GCMs include GW parameterizations. In general, GW parameterization schemes assume that GWs originate only from the lower atmosphere. In-situ generation of GWs in the middle atmosphere is ignored in these parameterizations. In addition, most standard GW parameterizations also assume that GWs propagate only vertically. However, using the KANTO model, Sato (2009; 2012) showed evidence of lateral propagation of GWs and provided theoretical explanations of the mechanisms involved. Conducting ray-tracing simulations, Yamashita et al. (2013) also suggested that high GW activity in the MLT during ES events observed by the Sounding of the Atmosphere using Broadband Emission Radiometry (SABER) on the Thermosphere, Ionosphere, Mesosphere Energetics Dynamics (TIMED) satellite is caused by poleward propagating GWs.

In this study, we used a high-top and GW-permitting GCM to examine an SSW-ES event that occurred in January 2019 in the actual atmosphere. We focused on the relative roles of GWs and PWs to elucidate the mechanism of the dynamical modification of the middle atmosphere during this event. Since GWs are explicitly resolved in the model, the in-situ generation and lateral propagation of GWs are also simulated. Three-dimensional analysis methods are also applied because zonal asymmetry is pronounced especially in the ES structures associated with displacement-type SSWs (Chandran et al., 2014; France and Harvey, 2013). The methods of analysis and details of the model used in this study are described in section 2. In section 3, the results are shown and discussed particularly in terms of the mechanism of the dynamical variation associated with the SSW. Characteristics of waves observed in the middle atmosphere are also shown. Summary and concluding remarks are given in section 4.

2 Methods and model description

In this study, we performed simulations of the 2018/19 SSW event using the Japanese Atmospheric General circulation model for Upper Atmosphere Research (JAGUAR) (Watanabe and Miyahara, 2009). The model has 340 vertical layers from the surface to a geopotential height of approximately 150 km with a log-pressure height interval of 300 m throughout the middle atmosphere and a horizontal, triangularly truncated spectral resolution of T639 that has a minimum resolvable horizontal wavelength of ~60 km. No parameterization for subgrid-scale GWs was used in this study.

The model resolutions are insufficient to resolve very small-scale GWs with horizontal wavelengths of < 60 km. Using observation data from the PANSY radar (Program of the Antarctic Syowa MST/IS radar) installed at Syowa Station (69.0° S, 39.6° E), Shibuya et al. (2017) and Shibuya and Sato (2019) showed the dominance of GWs with horizontal wavelengths in excess of 1,000 km and vertical wavelengths of about 14 km in the mesosphere. On the basis of PANSY radar observation data, Sato et al. (2017) showed that most GW momentum fluxes are associated with waves having long periods of several hours to a day at the southern high latitudes in summer. Ern et al. (2018) analyzed the satellite observation data and showed that dominant GWs in the middle atmosphere on average have horizontal wavelengths in excess of 1,000 km and vertical wavelengths in excess of 10 km. In addition, Watanabe et al. (2008) showed that a T213L256 GCM (the KANTO model) that explicitly resolves GWs can reproduce major characteristics of the zonal mean flow and temperature in the middle atmosphere. Thus, it is considered that the model used in this study is able to realistically resolve a major part of GWs in the middle atmosphere.

Koshin et al. (2020) recently developed a four-dimensional local ensemble transform Kalman filter (4D-LETKF) assimilation system in a medium-resolution (T42L124) version of the JAGUAR, and assimilated the PrepBUFR observational dataset provided by the National Centers for Environmental Prediction (NCEP) and satellite temperature data from the Aura Microwave Limb Sounder (MLS). They also improved the quality of the analysis data by introducing a filter called incremental analysis updates (Bloom et al., 1996) and assimilating the temperature data from SABER and brightness temperature data from Special Sensor

Microwave Imager/Sounder (SSMIS) (private communication). Using the products from the updated assimilation system from Koshin et al. (2020) as initial values for the high-resolution JAGUAR, a hindcast of the 2018/19 SSW event was carried out. The time period of simulation is from 5 December 2018 to 17 January 2019. This time period was divided into consecutive periods of 4 days. An independent model run was performed for each 4-day period. Each model run consists of 1-day nudging, 2-day spin up and 4-day free run. We analyzed the output data from the 4-day free runs.

The transformed Eulerian mean (TEM) primitive equations were used for diagnosing wave forcing and residual mean circulation (e.g., Andrews and McIntyre, 1976). In the TEM system, the Eliassen–Palm (EP) flux represents the direction of wave activity flux and its divergence (convergence) represents positive (negative) wave forcing. In addition, to visualize the longitudinal structure of residual mean circulation, we calculated three-dimensional residual mean vertical flow using the formula derived by Kinoshita et al. (2019):

$$\bar{w}^* = \bar{w} + \left(\frac{\overline{u_\mathrm{g}\theta}}{\theta_{0z}}\right)_x + \left(\frac{\overline{v_\mathrm{g}\theta}}{\theta_{0z}}\right)_y \tag{1}$$

where $\bar{A}$ denotes the time mean of A, and u_g and v_g are geostrophic zonal and meridional flows, respectively; the suffixes x and y denote the respective partial derivatives in the zonal and meridional directions; θ and θ_0 are the potential temperature and reference potential temperature, which is defined as $\theta_0 = (gH/R)e^{\kappa z/H}$; g represents the gravitational acceleration; H is scale height (= 7 km); R is the gas constant of dry air; κ is a dimensionless value and is defined as R/c_p, where c_p denotes specific heat at constant pressure. Equation (1) is the deformed form of the original equation of $\bar{w}^*$ in Kinoshita et al. (2019), using $[A]_x = 0$ and $[v_\mathrm{g}] = 0$, where $[A]$ denotes the zonal mean of A. This vertical flow contains the Stokes drift associated with transient and stationary waves. Moreover, apparent vertical motions along the undulated isentropic surfaces associated with the stationary waves are excluded. Thus, equation (1) represents the diabatic flow crossing the isentropic surfaces. In this study, we set the period of the time mean to four days.

To analyze three-dimensional wave propagation and forcing, we also used the two types of three-dimensional wave activity flux of Kinoshita and Sato (2013), namely 3D-flux-W and 3D-flux-M. The components of 3D-flux-W that are associated with the flux of zonal momentum are as follows:

$$\mathbf{F}_{W1} = \rho_0 \begin{pmatrix} \frac{1}{2}\left(\overline{u'^2} - \overline{v'^2} + \frac{\overline{\Phi_z'^2}}{N^2}\right) \\ \overline{u'v'} \\ \overline{u'w'} - f\frac{\overline{v'\Phi_z'}}{N^2} \end{pmatrix} \tag{2}$$

where ρ_0 denotes reference density. The 3D-flux-M is given as follows:

$$\mathbf{F}_1 = \rho_0 \begin{pmatrix} \overline{u'^2} - \overline{S_{(p)}} + \bar{u}_y \dfrac{\overline{S_{(p)}}}{f} - \bar{u}_z \dfrac{\overline{u'\Phi'_z}}{N^2} \\ \overline{u'v'} - \bar{u}_x \dfrac{\overline{S_{(p)}}}{f} - \bar{u}_z \dfrac{\overline{u'\Phi'_z}}{N^2} \\ \overline{u'w'} + -\bar{u}_x \dfrac{\overline{u'\Phi'_z}}{N^2} + \left(\bar{u}_y - f\right) \dfrac{\overline{v'\Phi'_z}}{N^2} \end{pmatrix} \tag{3}$$

where

$$S_{(p)} = \frac{1}{2}\left(\overline{u'^2} + \overline{v'^2} - \frac{\overline{u'\Phi'_y}}{f} + \frac{\overline{v'\Phi'_x}}{f}\right) \tag{4}$$

These formulae were originally derived for transient waves, but they hold for stationary waves if the wave component is extracted properly and an appropriate average is made (Sato et al., 2013). To analyze the wave activity fluxes associated with both transient and stationary PWs, we examined components having zonal wavenumbers s= 1–3 as the perturbation field and applied an extended Hilbert transform proposed by Sato et al. (2013) to eliminate phase dependency of waves instead of time averaging. Since the zonal mean flow is taken as the background field, $\bar{u}_x$ in the equation (3) is eliminated.

Kinoshita and Sato (2013) showed that the divergence of 3D-flux-M corresponds to the wave forcing that causes the three-dimensional residual mean flow, and 3D-flux-W agrees well with the direction of the group velocity of RWs. Thus, in the present study, we used the divergence of 3D-flux-M to examine the three-dimensional structure of wave forcing, and 3D-flux-W to analyze the characteristics of PW propagation. In the figures that follow, each component of $\mathbf{F}_{W1}$ is shown with the sign reversed to match the direction of the group velocity of RWs.

For the analysis of the dynamical stability of mean flow, we used the modified potential vorticity (MPV) defined by Lait (1994) as the Ertel's potential vorticity weighted by $\theta^{-9/2}$. In this paper, MPV is denoted by P_M. It roughly represents the product of absolute vorticity and the square of the Brunt–Väisälä frequency N^2 including perturbations (e.g., Sato and Nomoto, 2015).

3 Results and discussion

3.1 Overall features of the 2018/19 SSW event

The 2018/19 SSW event is classified as a displacement-type (s= 1) SSW and the onset of the major warming occurred on 1 January 2019. Figure 1 shows the time–height sections of zonal mean temperature $[T]$ and zonal wind $[u]$. Figure 1a shows temperature data from the MLS on the Aura satellite that have been bias-corrected with TIMED SABER data (Koshin et al., 2020). Figures 1b and 1c show model results. According to the model, the stratopause begins to descend from a climatological height of z= ~55 km in association with the SSW around 22 December 2018 (Fig. 1b). Zonal-mean zonal winds $[u]$ are reversed in the region of z= 40–80 km around 25 December (Fig. 1c). Following that, the stratopause and the peak of westward wind gradually descend to z= ~35 km.

A strong temperature maximum is formed at z= ~85 km around 28 December during the descent of the stratopause. This characteristic vertical structure of temperature with two peaks is referred to as the double stratopause (DS) in this study. After 10 January, the eastward wind is accelerated at z= ~65 km and the ES is at z= ~80 km. The heights of the DS and ES in the model are consistent with those indicated by the temperature data from the Aura MLS (Fig. 1a) within z= $\pm$5 km. The higher DS peak is located at z= ~90 km and the ES is at z= ~80 km in the Aura MLS data. Other temperature structures in the model results are generally consistent with the observation data. Note that the ES is separated from the upper stratopause of the DS.

Waves were divided into three components and analyzed separately: PWs having zonal wavenumber s= 1–3, medium-scale waves (MWs) having s> 3 and total horizontal wavenumber n< 21 and GWs having n= 21–639. Figure 2 shows the time–height sections of EP flux divergence (EPFD) [EPFD= $(\rho_0 a \cos\varphi)^{-1}\mathbf{\nabla}\cdot\mathbf{F}$, where a is the earth's radius and $\mathbf{F}$ is EP flux] for respective wave components. Positive (negative) EPFD represents eastward (westward) momentum deposit by waves. In the present study, 'positive (negative)' wave forcing means eastward (westward) momentum deposit. The EPFD was smoothed with a lowpass filter with a cutoff of one day. During 23–31 December including the period when the DS is present, GWF is strongly positive in the region of z= 65–90 km. Around the time of the formation of the DS, PWF takes a strongly negative value of ~$-$50 m s^{-1} d^{-1} above z= 83 km. This negative PWF likely contributes to DS formation. Around 10 January when the ES is formed, GWF and PWF are negative above z= 70 km and 80 km, respectively, suggesting that both negative wave forcings are responsible for ES formation. The mechanisms of the formation of the DS and ES are discussed in detail in sections 3.2. Because forcing by MWs is always weak at any height or time, the following sections focus only on PWF and GWF.

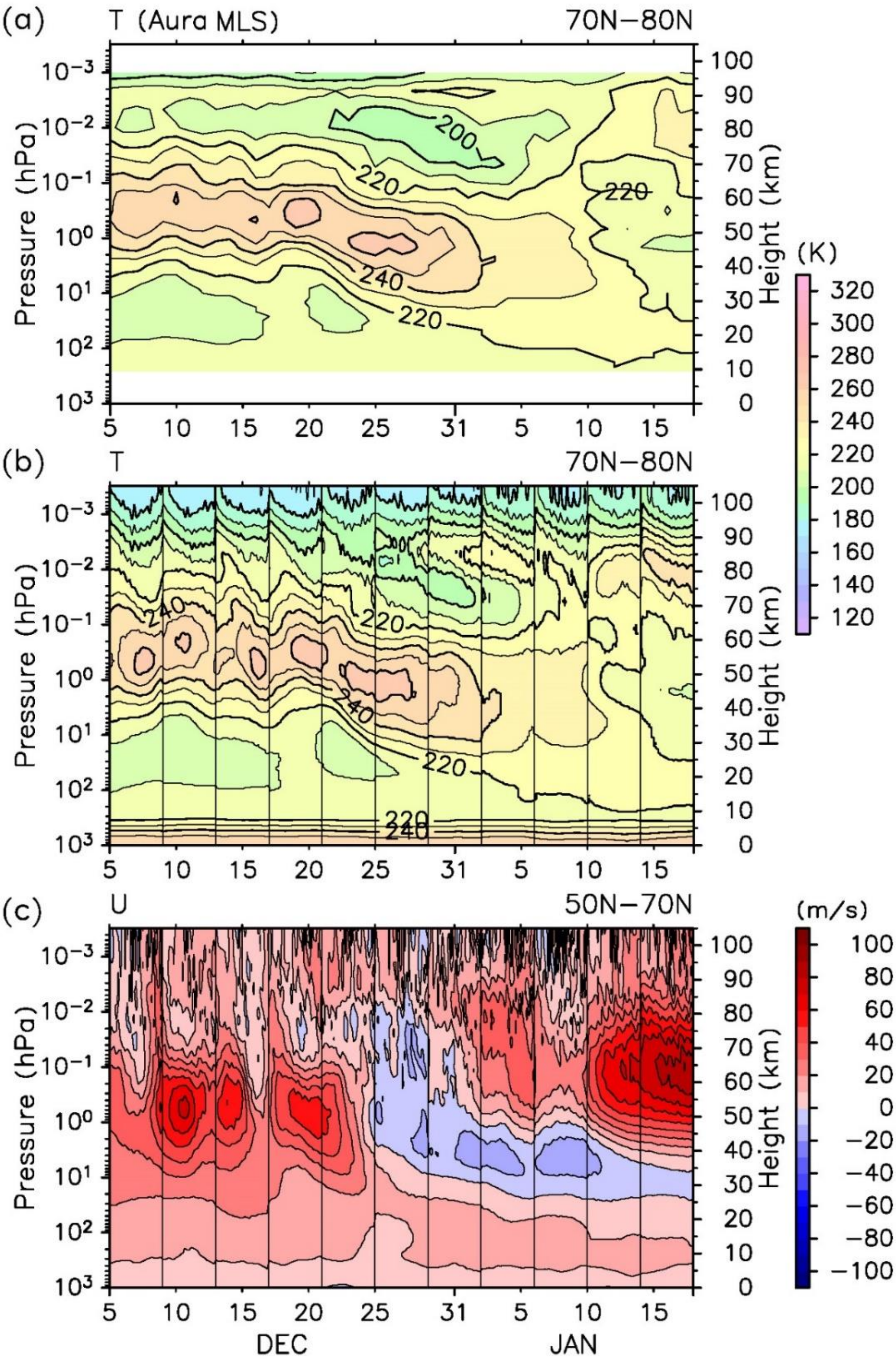

Figure 1. Time–height sections of 70° N–80° N regional mean $[T]$ from (a) the Aura MLS and (b) JAGUAR-T639L340 simulation, and (c) 50° N–70° N regional mean $[u]$ from the JAGUAR-T639L340 simulation. Vertical lines in (b) and (c) represent the boundaries of the model runs.

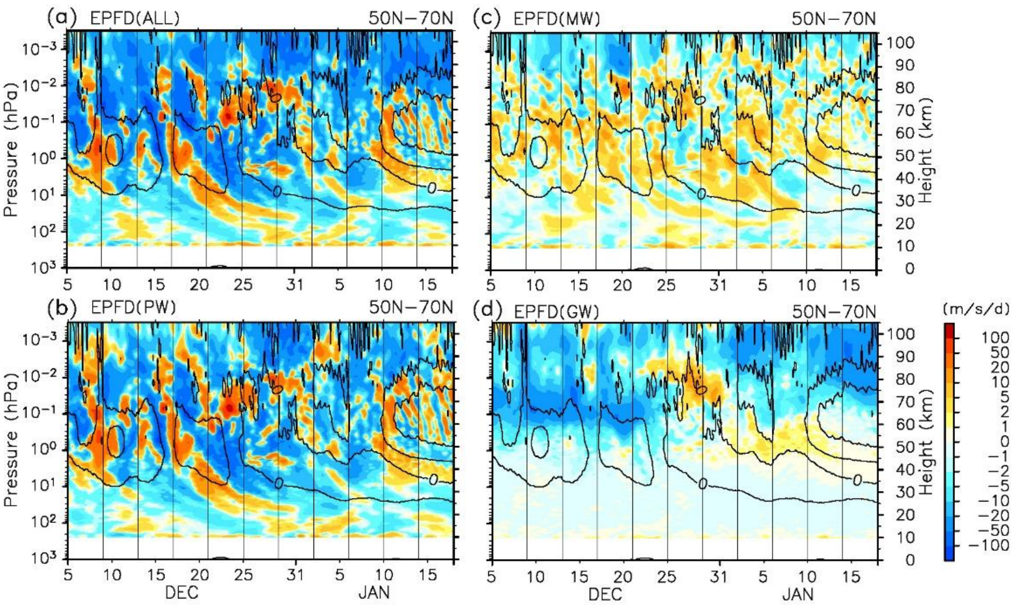

Figure 2. Time–height sections of 50° N–70° N regional mean EPFD of (a) all wave components, (b) PW, (c) MW, and (d) GW (shadings) and 50° N–70° N regional mean $[u]$ (contour interval: 20 m s^{-1}). Vertical lines represent the boundaries of the model runs.

3.2 Mechanisms of the formation of the DS and ES

To elucidate the mechanisms of the formation of the DS and ES, time evolutions of the zonal mean fields and horizontal structures of the mean flow and wave forcing are examined in this section.

3.2.1 The formation of the DS during 25–28 December 2018

3.2.1.1 Meridional cross section

Figure 3 shows the meridional cross sections of zonal mean and four-day mean fields of temperature, zonal wind, MPV, and EP flux and EPFD of PWs and GWs for 17–20, 21–24 and 25–28 December 2018. The DS is formed around 28 December (Figs. 1a and 1b). To accentuate vectors in the middle atmosphere, EP flux vectors are devided by $\rho_0 a$ in all the figures. In 17–20 December, there is a strong eastward polar night jet, and its axis is at ~50° N and z= ~52 km (Fig. 3a). Westward wind is observed equatorward of this eastward jet; GWF is strongly negative up to ~50 m s^{-1} d^{-1} at ~50° N and z= ~65 km above the eastward jet, and positive above the westward wind region. These GWF features are likely results of the filtering effect by the eastward and westward mean wind below.

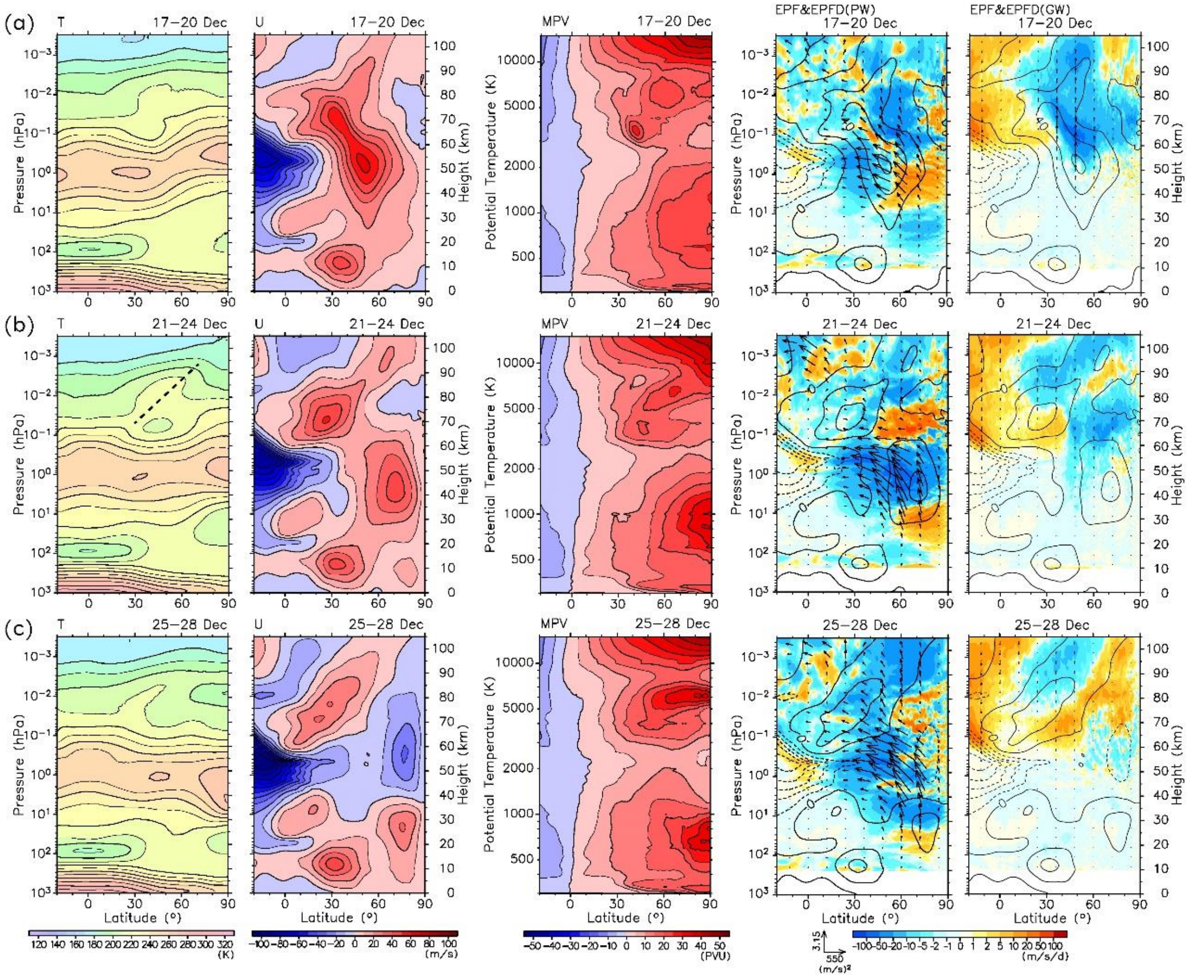

Figure 3. Latitude–height sections of (from left to right) 4-day mean $[T]$, $[u]$, $[P_M]$ and EP flux scaled by $\rho_0 a$ (vectors) and EPFD (shadings) of PWs and GWs for (a) 17–20, (b) 21–24, and (c) 25–28 December 2018. Contours in the figures of EP flux and EPFD denote $[u]$ (contour interval = 20 m s^{-1}). A dashed line in the temperature figure in (b) shows the region with relatively high temperature in the mesosphere (see section 3.2).

There is a notable peak of $[P_M]$ at ~40° N and θ= ~3,500 K (z= ~65 km), which is located on the boundary between the negative and positive GWFs. Wave-induced residual mean vertical wind is upward in the lower region on the poleward (equatorward) side of positive (negative) wave forcing. These GWF and $[P_M]$ features suggest that the $[P_M]$ peak is a result of an increase in N^2 above the residual mean upward flow at ~40° N (not shown, cf. section 3.2.1b), which is induced by the positive and negative GWFs.

During 17–20 December, PWF is positive poleward of ~55° N at z= 35–55 km; PW packets propagate toward the region with weak $[u]$ at ~30° N, z= 40–65 km and toward 40° N–70° N, z= 60–85 km by way of the eastward jet, which has its axis at ~50° N, z= ~52 km. In both regions, PWF is negative. The negative PWF in the latter region may also contribute to the upwelling at ~40° N and the increase in N^2 and $[P_M]$. However, the boundary of the positive and negative total wave forcing (not shown) match well with that of the positive and negative GWFs. Thus, the location and strength of the upwelling are mainly determined by the GWFs.

During 21–24 December, the eastward jet is split into two segments. One segment is shifted poleward and downward and located at ~72° N, z= ~42 km and the other segment tilts poleward from the equator at z= ~65 km to the winter pole at z= ~100 km with its axis at ~25° N, z= ~72 km (Fig. 3b). This segmentation of the jet may be caused by negative GWF and PWF that are present during 17–20 December in the region where the split occurs. During 21–24 December, GWF is negative (positive) above (below) the latter, poleward-tilting eastward jet, and is consistent with the GW filtering effect of this jet. The temperature cross section shows relatively high temperature between 30° N, z= ~70 km and 70°N, z= ~95 km. The region with relatively high temperature is marked by a dashed line in Fig. 3b and corresponds to the area between the negative and positive GWFs along the mesospheric jet. This fact suggests that the high temperature is caused by adiabatic heating associated with residual mean downwelling (not shown) induced by these GWFs.

Poleward of 10° N in the middle and upper stratosphere at z= 35–60 km during 21–24 December, PWF is strongly negative with a maximum of over 50 m s^{-1} d^{-1}, and is present continuously until 25–28 December (Fig. 3c). It is inferred that the SSW is caused by this PWF. During 21–24 December, PWF is positive to the north of ~40° N at z= 60–80 km (Fig. 3b), and the $[P_M]$ peak that is present during 17–20 December at ~40° N and θ= ~3,500 K becomes weak. According to the quasi-geostrophic theory, a positive EPFD is equivalent to a poleward PV flux, while a negative EPFD indicates an equatorward PV flux (Andrews et al., 1987). The observed PWF features suggest that the positive wave forcing is associated with the PW generation due to the BT/BC instability weakening the negative $[P_M]_y$, which is a necessary condition for the BT/BC instability. During this period, a $[P_M]$ peak becomes obvious from ~50° N, θ= ~5,500 K (z= ~80 km) to ~80° N, θ= ~7,000 K (z= ~85 km). It is slightly below the region with relatively high temperature, which is marked by the dashed line in Fig. 3b. Thus, it is implied that this $[P_M]$ peak is caused by the increase of N^2 under the temperature maximum associated with the isothermal folding.

During 25–28 December, a westward jet with a peak at z= ~57 km, ~80° N is formed in the polar upper stratosphere and mesosphere (Fig. 3c). The stratopause shifts downward from z= ~52 km in 21–24 December to z= 38 km corresponding to the SSW. A relatively weak maximum in the vertical profile of $[T]$ is formed to the north of 60° N at z= ~88 km. This structure with two maxima in the vertical profile is the DS. Poleward of 55° N at z= 67–82 km, where the $[P_M]_y$ is negative in 21–24 December, PWF becomes positive during 25–28 December and the $[P_M]_y$< 0 region almost disappears. These results suggest in-situ

PW generation due to the BT/BC instability at z= 67–82 km during 25–28 December, which is similar to the model results at > 40° N, z= 60–80 km from 21–24 December.

During 25–28 December, a negative PWF of ~−20 m s^{-1} d^{-1} extends to the north of 35° N above z= 85 km, and a positive GWF of ~10 m s^{-1} d^{-1} is in the polar MLT. Because the positive GWF is weaker than the negative PWF, the total wave forcing is negative in the polar MLT (z> 80 km) (Fig. 2a). Thus, the negative PWF at the middle and high latitudes in the MLT is responsible for DS formation by causing downwelling in the polar MLT and the subsequent adiabatic heating.

During 25–28 December, the mean zonal wind is westward over a wide area above z> 40 km in the polar upper stratosphere and mesosphere. According to the Charney and Drazin theorem (1961), PWs from the troposphere hardly propagate upward in the westward wind and reach the MLT. Thus, it is inferred that the in situ generated PWs propagate upward and exert negative forcing in the MLT, leading to the formation of the DS.

3.2.1.2 Horizontal structure

To analyze the horizontal structures of P_M and wave forcing, orthographic projection maps of the Northern Hemisphere for P_M, geopotential height (GPH), N^2, u, $-du^{\dagger}w^{\dagger}/dz$ due to GWs, where $\dagger$ denotes the GW components, and the vertical gradient of residual mean vertical flow $d\overline{w}^{*}/dz$ at θ= ~3,500 K and 0.1 hPa (z= ~65 km) during 17–20 December are shown in Fig. 4a. The maps for $-du^{\dagger}w^{\dagger}/dz$ and $d\overline{w}^{*}/dz$ fields have been smoothed with a lowpass filter with a cutoff of s= 6 to show the large-scale structures more clearly. Calculations of $d\overline{w}^{*}/dz$ were performed using $\overline{w}^{*}$ at $\pm$5 km adjacent vertical levels; $-du^{\dagger}w^{\dagger}/dz$ approximately corresponds to GWF, and P_M is roughly proportional to the product of absolute vorticity $f+\zeta$ and N^2 (Sato and Nomoto, 2015).

The region of high P_M at ~40° N, which corresponds to the region of $[P_M]$ maximum in Fig. 3a, matches with the region of high N^2 and does not match with the region of the center of the polar vortex in the GPH maps. High N^2 is distributed along a strip at ~40° N, 0°–150° E, between the regions of strongly positive and negative GWFs near the eastward jet. The strongly negative $d\overline{w}^{*}/dz$, which is located above strong upwelling at ~0.2 hPa (z= ~60 km) (not shown), is observed at almost the same latitudes and longitudes as high N^2. These features indicate that the $[P_M]$ enhancement in the zonal mean field (Fig. 3a) is mainly caused by N^2 increase in the region of $\overline{w}^{*}$ convergence at the top of the upwelling induced by GWF, and is similar to the mechanism shown by Sato and Nomoto (2015).

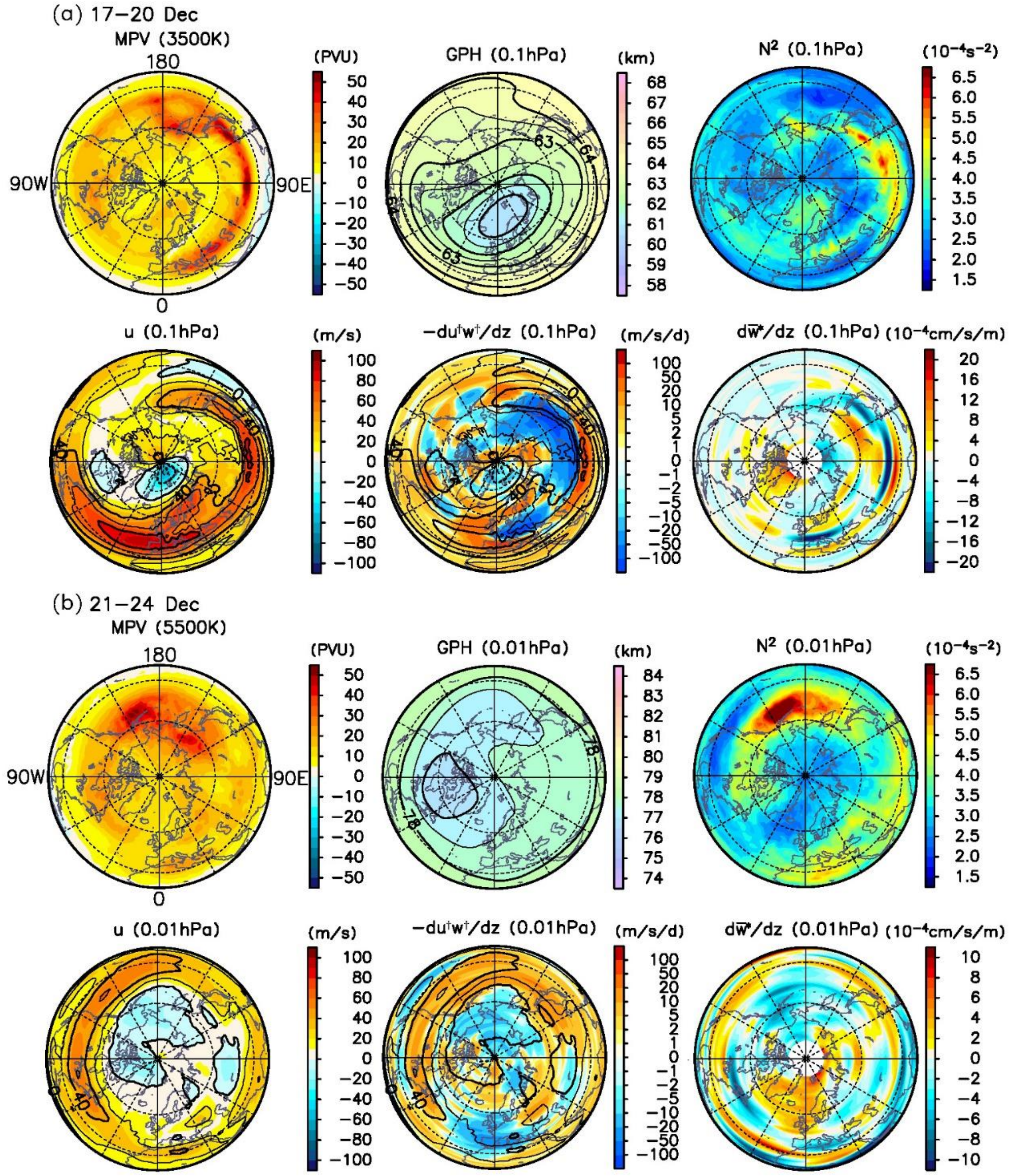

Figure 4. Orthographic projection maps of the Northern Hemisphere showing 4-day mean (top left to bottom right) P_M, GPH, N^2, u, $-du^\dagger w^\dagger/dz$, and $d\overline{w}^*/dz$ at (a) 0.1 hPa and θ= 3,500 K (z= ~65 km) for 17–20 December 2018 and (b) 0.01 hPa and θ= 5,500 K (z= ~80 km) for 21–24 December 2018. Contours in the figures of $-du^\dagger w^\dagger/dz$ denote u (contour interval = 20 m s^{-1}). The maps for $-du^\dagger w^\dagger/dz$ and $d\overline{w}^*/dz$ have been zonally smoothed with a lowpass filter with a cutoff of s= 6. Note that the color bar of $d\overline{w}^*/dz$ in (a) is different from that in (b).

Figure 4b shows orographic projection maps of P_M, GPH, N^2, u, $-du^\dagger w^\dagger/dz$ and $\overline{w}^*$ for 21–24 December at θ= ~5,500 K and 0.01 hPa (z= ~80 km) in the Northern Hemisphere. Similar to the period of 17–20 December, the region of high P_M at ~50° N, 120° E–120° W roughly corresponds to the region of high N^2. For the region of $\overline{w}^*$ convergence (divergence), N^2 is high (low), and $\overline{w}^*$> 0 lies below and $\overline{w}^*$< 0 lies above (not shown). The region of convergence is located near the region of strongly positive GWF (i.e., positive $-du^\dagger w^\dagger/dz$), which is found along the eastward jet. In addition, negative GWF is found equatorward of the region of positive GWF. The zonal mean of these GWFs are tilted toward the higher latitudes at the same altitudes as the tilted mesospheric eastward jet (Fig. 3b). The residual mean downward flow is induced between the negative and positive GWFs, while the residual mean upward flow is below and poleward of the positive GWF. Thus, it is inferred that the region of $\overline{w}^*$ convergence near the positive GWF is caused by this residual mean flow structure. The features observed in the maps support the inference from the zonal mean fields that the P_M peak is formed as a result of N^2 increase induced by the convergence of the residual mean vertical flow, which is caused by the pair of negative and positive GWFs around the mesospheric eastward jet.

3.2.2 The formation of the ES during 10–13 January, 2019

3.2.2.1 Meridional cross section

To examine the mechanism of ES formation, latitude–height sections of $[T]$, $[u]$, $[P_M]$ and EP flux and EPFD of PWs and GWs after the SSW onset on 1 January for the time periods of 2–5, 6–9 and 10–13 January are shown in Fig. 5. The ES becomes visible at z= ~80 km to the north of 70° N during 10–13 January (Fig. 5c). The upper $[T]$ maximum in the polar MLT is 220–230 K during 2–5 January, which is higher than the upper maximum (200–210 K) of the DS during 25–28 December (Fig. 3c). During 2–5 January, GWF is strongly negative above z= 80 km to the north of 20° N. This forcing probably acts to reinforce the DS structure by causing downwelling in the polar MLT. During 2–5 January, the zonal mean zonal wind $[u]$ is westward in the winter polar stratosphere and eastward in the mesosphere. According to the Charney and Drazin theorem (1961), the westward wind in the stratosphere prevents the upward propagation of PWs from the troposphere. Model results show that PWF through the stratosphere and mesosphere is weaker (but negative) after the SSW onset, when the zonal wind is westward in the polar stratosphere.

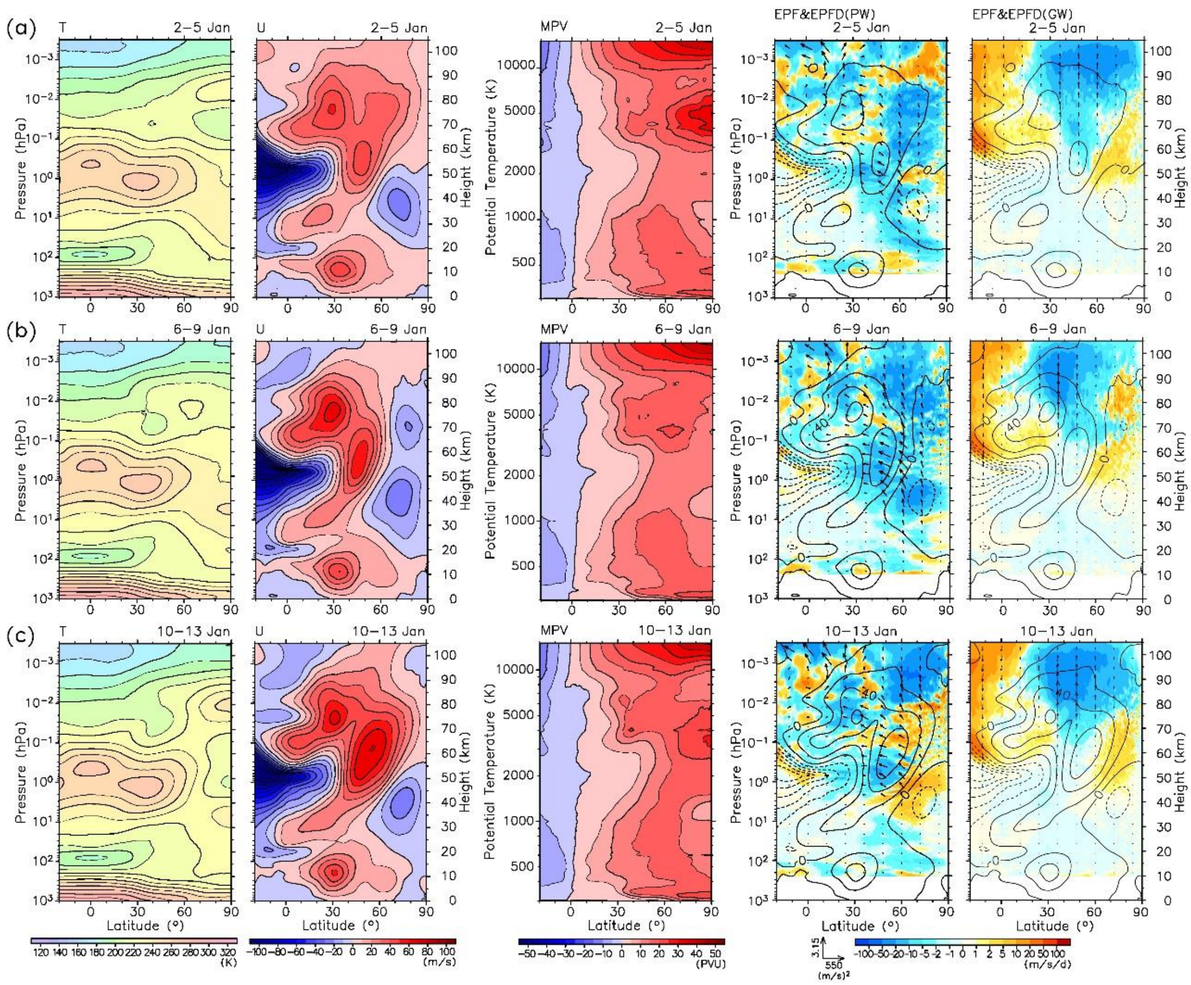

Figure 5. Same as Fig. 3 but for (a) 2–5, (b) 6–9 and (c) 10–13 January 2019.

During 6–9 January, the prevailing PWF through the entire winter polar middle atmosphere is negative with values of about -10 to -20 m s^{-1} d^{-1} (Fig. 5b). A westward wind is dominant in the polar mesosphere. After the SSW onset, it has descended to the stratosphere, and is reformed during 6–9 January. Thus it is implied that the reformation of the mesospheric westward wind is caused by this negative PWF. In the $[P_M]$ cross section, there is a peak at ~60° N and θ= 3,000–6,000 K (z= 60–80 km), below which is a weak $[P_M]$ peak at ~60° N in the stratosphere at θ= 500–2,000 K (z= 22–50 km). The weak peak is formed during 25–29 December, just before the onset of the major warming on 1 January (not shown). This peak is likely to be caused by negative PWF associated with the SSW. During 6–9 January, another weak peak also appears at ~40° N and θ= 4,000–6,000 K (z= 70–80 km).

During 6–9 January, PWs propagate upward into the mesosphere despite the westward wind below in the polar stratosphere. According to the Charney and Drazin theorem (1961), RWs hardly propagate in a westward wind region. In the meridional cross section of $[P_M]$ of

2–5 January (Fig. 5a), there is a maximum at ~60° N in the stratosphere (θ= 600–1,100 K). On the poleward side of this maximum, the necessary condition for the BT/BC instability (i.e., $[P_M]_y$< 0) is fulfilled. The region of negative $[P_M]_y$ is continuously maintained for a long time over the periods of 6–9 and 10–13 January (Figs. 8b and 8c) after 2–5 January. However, significant positive PWF, which suggests PW generation, is not observed during the period of 2–5 January or 6–9 January (Figs. 8a and 8b). Thus, we need a different mechanism from generation in the middle atmosphere to explain PWs propagating into the upper mesosphere during 6–9 January.

We examined the longitudinal characteristics of PW propagation from the upper troposphere to the mesosphere during 6–9 January. The longitude-height sections of the 3D-flux-W $\mathbf{F}_{W1}$ from Kinoshita and Sato (2013) averaged over 60° N–70° N for 6–9 January are shown in Fig. 6. The vectors represent the zonal and vertical components of the flux, the shading represent the vertical components of $\mathbf{F}_{W1}$ and the contours represent the zonal wind averaged over 60° N–70° N at each longitude. To show the vertical structure more clearly, $\mathbf{F}_{W1}$ is weighted by $\rho_0^{-1/2}$.

The upward propagation of waves occurs mainly in the region of 60° W–60° E, where the zonal wind has a westward tilting structure at z= 20–55 km. This westward tilting structure is consistent with the structure of upward propagating RWs and similar structure was observed during the major SSW in February 2018 (e.g., Harada et al., 2019). Thus, the westward winds in this region can be regarded as part of the PWs. It is inferred that waves propagate upward in the region of 60° W–60° E, even though the zonal mean zonal wind is westward.

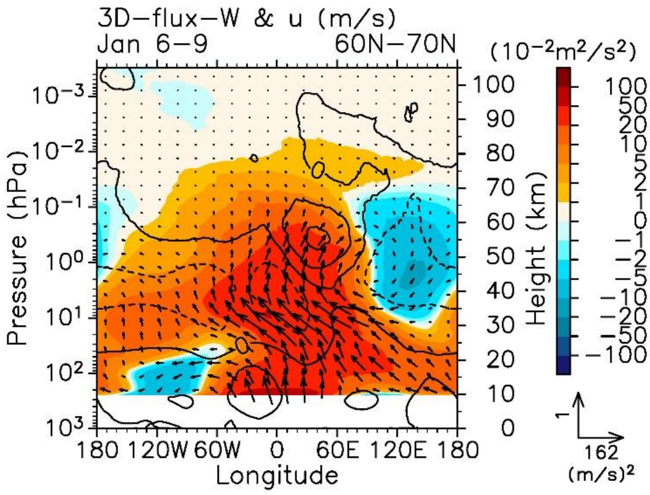

Figure 6. Longitude–height section of the 3D-flux-W $\mathbf{F}_{w1}$ weighted by $\rho_0^{1/2}$ (shading and vectors) averaged over 60° N–70° N for 6–9 January 2019. Shading indicates the vertical component of $\mathbf{F}_{w1}$. Solid contours indicate u averaged over the same region (contour interval = 20 m s^{-1}). Dashed contours indicate negative values.

As seen in Fig. 5c, during 10–13 January, the eastward jet becomes stronger and extends to the polar mesosphere. The PWs and GWs provide strong negative forcing at z> 80 km poleward of 50° N and 20° N, respectively. There is a $[T]$ maximum corresponding to the ES poleward of ~60° N at z= ~80 km. Thus, it is considered that both negative PWF and GWF are responsible for ES formation by causing downwelling below and poleward of the forcing regions.

The $[P_M]$ maximum at ~40° N and θ= 3,500–6,000 K (z= 65–80 km), which is already present during 6–9 January, is enhanced in 10–13 January. It is at ~38° N, θ= ~4,000 K (z= ~70 km) and is sandwiched between negative and positive GWFs. The GWFs lead to the formation of the $[P_M]$ peak at ~38° N, θ= ~4,000 K (z= ~70 km) via a similar process that leads to the formation of the $[P_M]$ peak at ~40° N, θ= ~3,500 K (z= ~65 km) during 17–20 December. The negative or near zero $[P_M]_y$, which is poleward of ~60° N and over the wide region of θ= 500–6,000 K (z= 22–80 km) during 6–9 January, has disappeared from θ= 1,200–6,000 K (z= 40–80 km) in 10–13 January (Fig. 5c). During 10–13 January, PWF is strong and positive poleward of 60° N at z= 35–80 km. This region of positive PWF roughly matches the region where the negative $[P_M]_y$ in 6–9 January becomes positive in 10–13 January. These features suggest in-situ PW generation due to the BT/BC instability.

3.2.2.2 Horizontal structure

To examine the formation of the $[P_M]$ peak at ~60° N, θ= 3,000–6,000 K (z= 60–80 km) during 6–9 January in terms of the horizontal structure, orthographic projection maps of P_M, GPH and N^2 at θ= ~4,000 K and 0.05 hPa (z= ~70 km) for 6–9 and 10–13 January are shown in Fig. 7. In contrast to the results from 17–20 and 21–24 December (Fig. 4), high P_M, low GPH (i.e., the center of the polar vortex) and high N^2 appear roughly in the same regions. During 6–9 January, the polar vortex is shifted equatorward at ~135° W. The region of low GPH is stretched and distorted into a comma-like shape at ~60° E. This is a typical structure for PW breaking. Thus, it is inferred that the mixing caused by PW breaking eliminates the P_M minimum at ~60° E associated with the polar vortex shift, and only the P_M maximum at ~135° W remains in the zonal mean field $[P_M]$. During 10–13 January, the polar vortex and the P_M maximum approach the pole, corresponding to the elimination of $[P_M]_y$< 0 in the zonal mean field (Figs. 5b and 5c). High P_M is distributed along a strip at ~40° N, and corresponds to the weak $[P_M]$ peak at ~38° N, θ= ~4,000 K (z= ~70 km) between negative and positive GWFs (Figs. 5b and 5c).

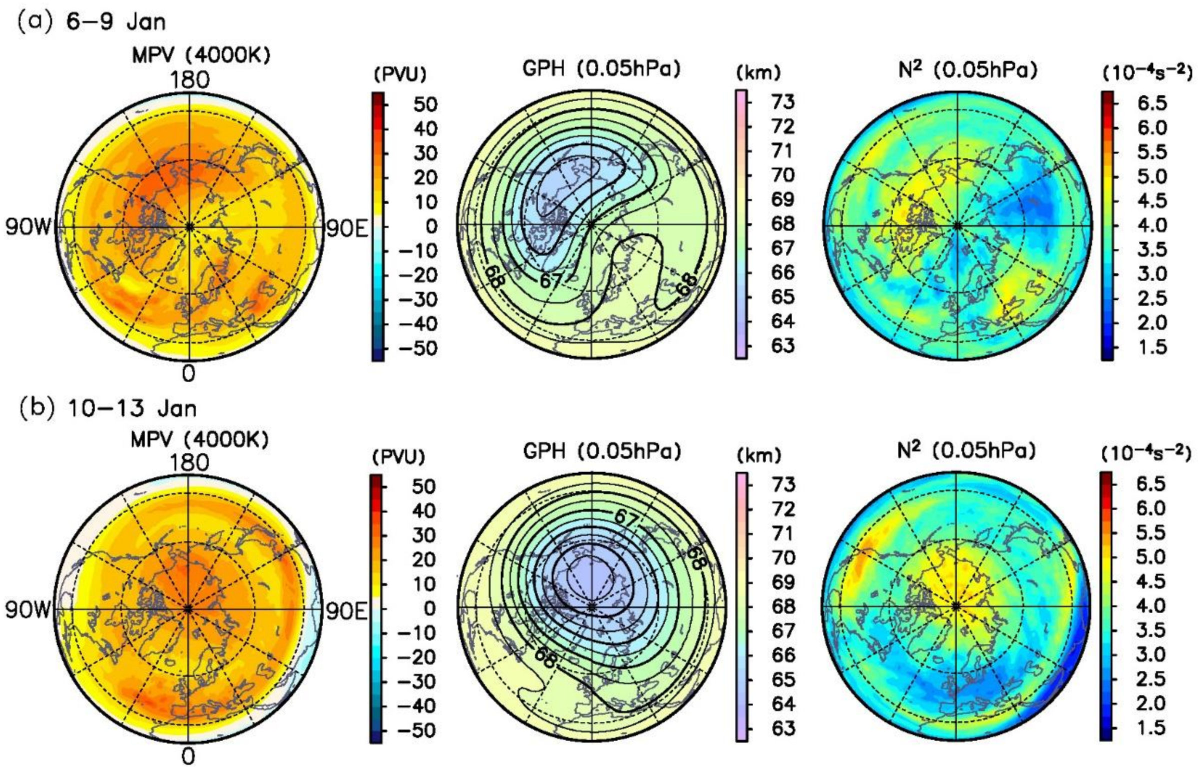

Figure 7. Orthographic projection maps of the Northern Hemisphere showing 4-day mean (left to right) P_M, GPH and N^2 at 0.05 hPa and θ= 4,000 K (z= ~70 km) for (a) 6–9 and (b) 10–13 January 2019.

During 10–13 January when the ES is formed, PWs from the troposphere hardly reach the polar MLT because of the prevailing westward wind in the polar stratosphere (Fig. 5c). Thus, it is considered that the negative PWF, which is responsible for ES formation together with the negative GWF, is caused by the breaking of PWs that are generated in the mesosphere (via the process discussed above) propagating into the MLT. The recovered mesospheric eastward jet provides an environment in which these in-situ generated PWs can propagate vertically. The recovered eastward jet also affects GW propagation through its filtering effect.

3.2.2.3 Zonal asymmetry of the ES

As shown in previous studies (e.g., France and Harvey, 2013), the ES has zonal asymmetry especially after displacement-type SSWs such as the 2018/19 event. Figure 8 shows the GPH map at 0.01 hPa (z= ~80 km) during 10–13 January and the time–height sections of the temperature at 70° N latitude and longitudes of 30° E, 75° E, 120° E, 165° E, 150° W, 105° W, 60° W and 15° W. The ES, i.e., a temperature maximum at z= ~80 km that appears around 10 January, is present at 75° E, 120° E, 165° E, 150° W and 105° W (as denoted by yellow and orange stars in the GPH map). However, its presence at 60° W, 15° W and 30° E is unclear (open stars). The clearest and strongest ES structure appears at 70° N, 150° W (an orange star). The sites where the ES is observed are located inside of the polar vortex. Thus, it is indicated that the ES is not an apparent phenomenon that is only seen in the zonal mean field associated with a shift of the polar vortex, but is a real warming of the atmosphere inside of the polar vortex.

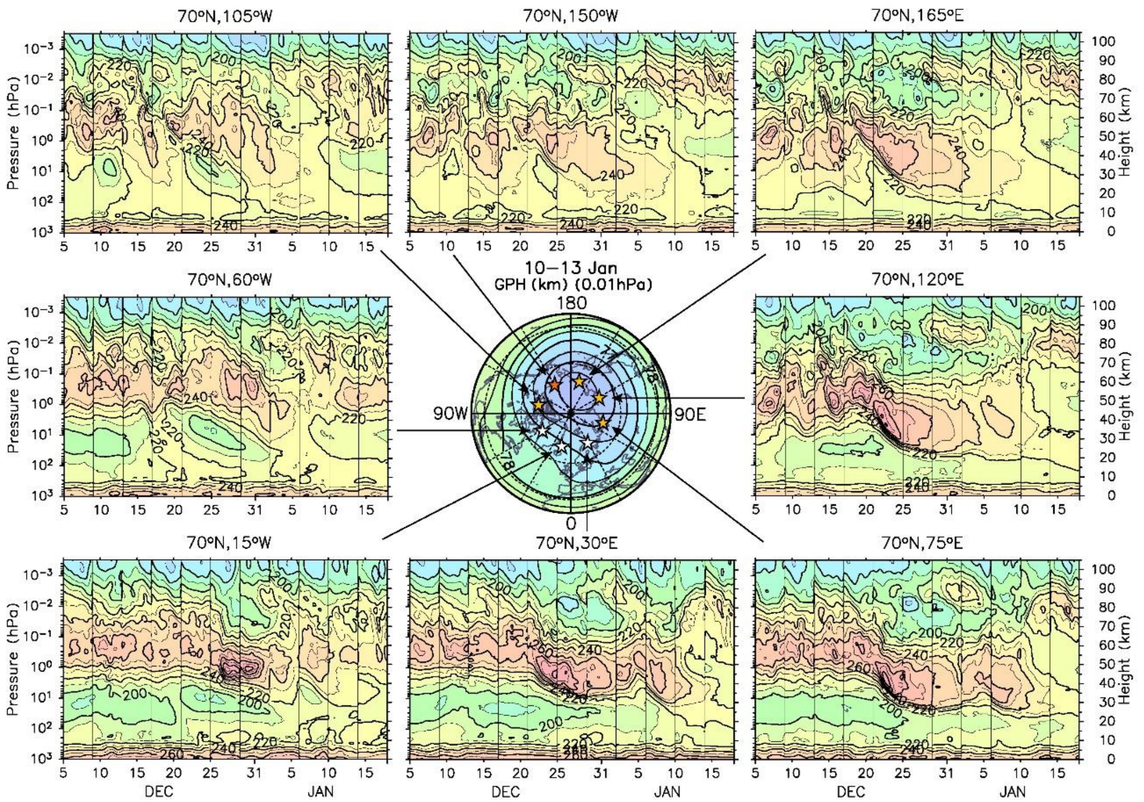

Figure 8. An orthographic projection map of the Northern Hemisphere showing 4-day mean GPH (unit: km) at 0.01 hPa for 10–13 January 2019 and time–height sections of T (unit: K) smoothed with a lowpass filter with a cutoff of one day at a latitude of 70° N and longitudes of 30° E, 75° E, 120° E, 165° E, 150° W, 105° W, 60° W and 15° W. Star symbols in the GPH map denote the locations for the T figures. Vertical lines in the T figures represent the boundaries of the model runs.

Figure 9 shows the maps of $\overline{w}^*$ at 0.01 hPa (z= ~80 km), u at 0.05 hPa (z= ~70 km), and $-du^\dagger w^\dagger/dz$ due to GWs and $-\rho_0^{-1}(\nabla \cdot \mathbf{F}_1)$ due to PWs at 0.002 hPa (z= ~92 km), which correspond to GWF and PWF, respectively. Downward flow at 70° N latitude is weak in the region of 30° W–0°–60° E and strong in the region of 90°E–180°–135°W (Fig. 9a). The GWF is negative at 30° N–60° N, 120° E–180°–60° W (Fig. 9c), and positive inside of the eastward jet streak extending from 45° N, 30° W to 70° N, 180°. The PWF at 50° N–80° N, 30° E–180°–90° W is strongly negative, with values below -100 m s^{-1} d^{-1} (Fig. 9d). At 90° W–0°–30° E, PWF is positive poleward of 60° N.

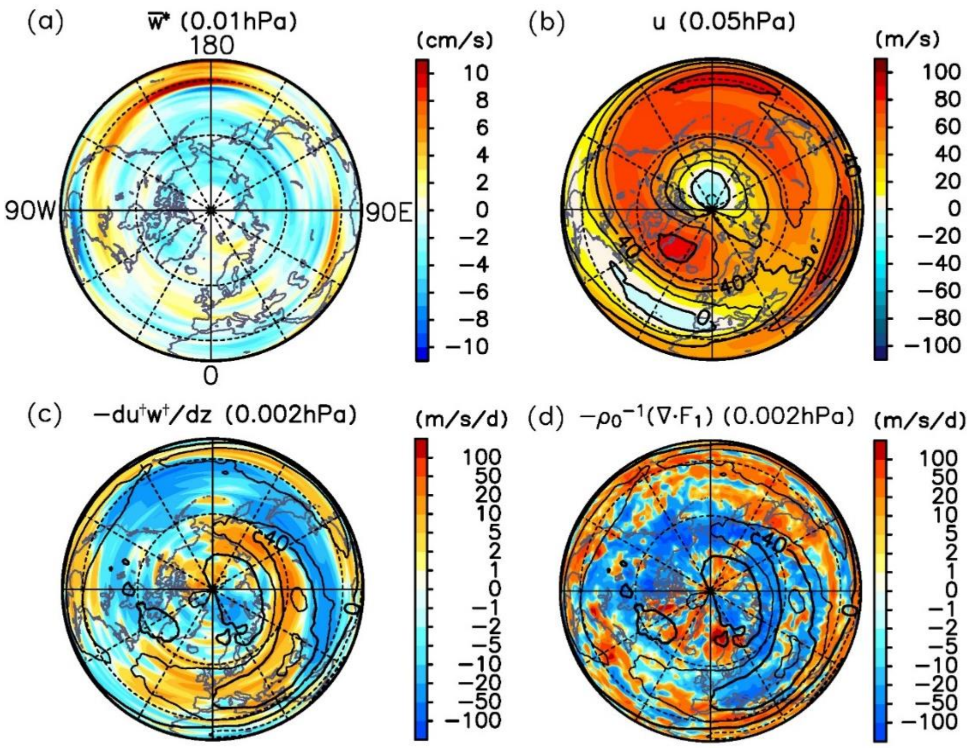

Figure 9. Orthographic projection maps of the Northern Hemisphere showing 4-day mean (a) $\overline{w}^{*}$ at 0.01 hPa, (b) u at 0.05 hPa, (c) $-du^{\dagger}w^{\dagger}/dz$ due to GWs at 0.002 hPa and (d) $-\rho_0^{-1}(\nabla\cdot\mathbf{F}_1)$ due to PWs at 0.002 hPa for 10–13 January 2019. Note that $\overline{w}^{*}$ and $-du^{\dagger}w^{\dagger}/dz$ are zonally smoothed with a lowpass filter with a cutoff of s= 6.

Equatorward of the region at around 70° N, 150° W, where the ES is clear and strong, both GWF and PWF are negative. In contrast, at 60° W–30° E, where the ES is very weak or absent, GWF and PWF are positive equatorward and poleward of ~60° N, respectively. The net forcing of these two waves is positive in this region. Negative (positive) net wave forcing induces downward (upward) flow poleward. Thus, it is inferred that the asymmetric ES is caused by vertical flow induced by the zonally asymmetric wave forcing.

Why are GWF and PWF positive at 60° W–30° E? At 0.05 hPa (z= ~70 km), where the eastward jet is recovered in the polar mesosphere (see Fig. 5c), eastward wind is particularly strong poleward of 50° N (Fig. 9b). Equatorward of this eastward wind, a weak westward wind appears. This recovered mesospheric eastward jet provides suitable conditions for upward propagation of PWs and westward GWs. However, it is implied that PWs are refracted and are unable to propagate upward at >60° N, 60° W–30° E because eastward winds are too strong in this region. In addition, the westward wind at <60° N, 60° W–30° E prevents upward propagation of PWs as well as westward GWs through its filtering effect. Thus, it is inferred that this u structure prevents the appearance of negative GWF and PWF in the MLT above.

3.3 Characteristics of PWs generated in the middle atmosphere

To examine the characteristics of PWs that are generated in the middle atmosphere via the processes described in section 3.2, the longitude–time section of GPH deviation from zonal mean at 60° N–70° N, z= 80 km is shown in Fig. 10a. During 21–24 December, PWF is positive north of ~40° N at z= 60–80 km (Fig. 3b) and stationary PWs with s= 1 are dominant. During 25–28 December, PWF is positive poleward of 55° N at z= 67–82 km, the DS is formed (Fig. 3c) and westward propagating PWs have periods of ~6 days (indicated by the dashed line in Fig. 10a) and s= 1–2. During 10–13 January, when the ES is formed, PWs have periods of ~24 days (the dash-dotted line) and s= 1.

Figures 10b, 10c and 10d show the longitude–height sections of GPH deviation and the 3D-flux-W $\mathbf{F}_{W1}$ on 21, 26 December and 10 January, respectively. On 21 December, the westward tilting structure of GPH and upward propagation indicated by $\mathbf{F}_{W1}$ associated with waves from the troposphere are attenuated at z= ~55 km (Fig. 10b). This is because the wave packet from the lower atmosphere propagates equatorward below this level (see Fig. 3b). The westward tilting structure of GPH and positive vertical component of $\mathbf{F}_{W1}$ are also present above z= ~65 km; as discussed in section 3.2, these features are associated with PWs that are generated by the BT/BC instability in the middle atmosphere.

On 26 December (Fig. 10c) and 10 January (Fig. 10d), layers with $[u]$< 0 m s^{-1} are observed at z= 43–85 km and 20–53 km, respectively. In these layers, upward wave propagation is markedly attenuated. The features suggesting upward wave propagation (i.e., westward tilting structure of GPH and a positive vertical component of $\mathbf{F}_{W1}$) are present at higher altitudes. For both 26 December and 10 January, PWs having s= 1 are dominant in the regions of upward wave propagation.

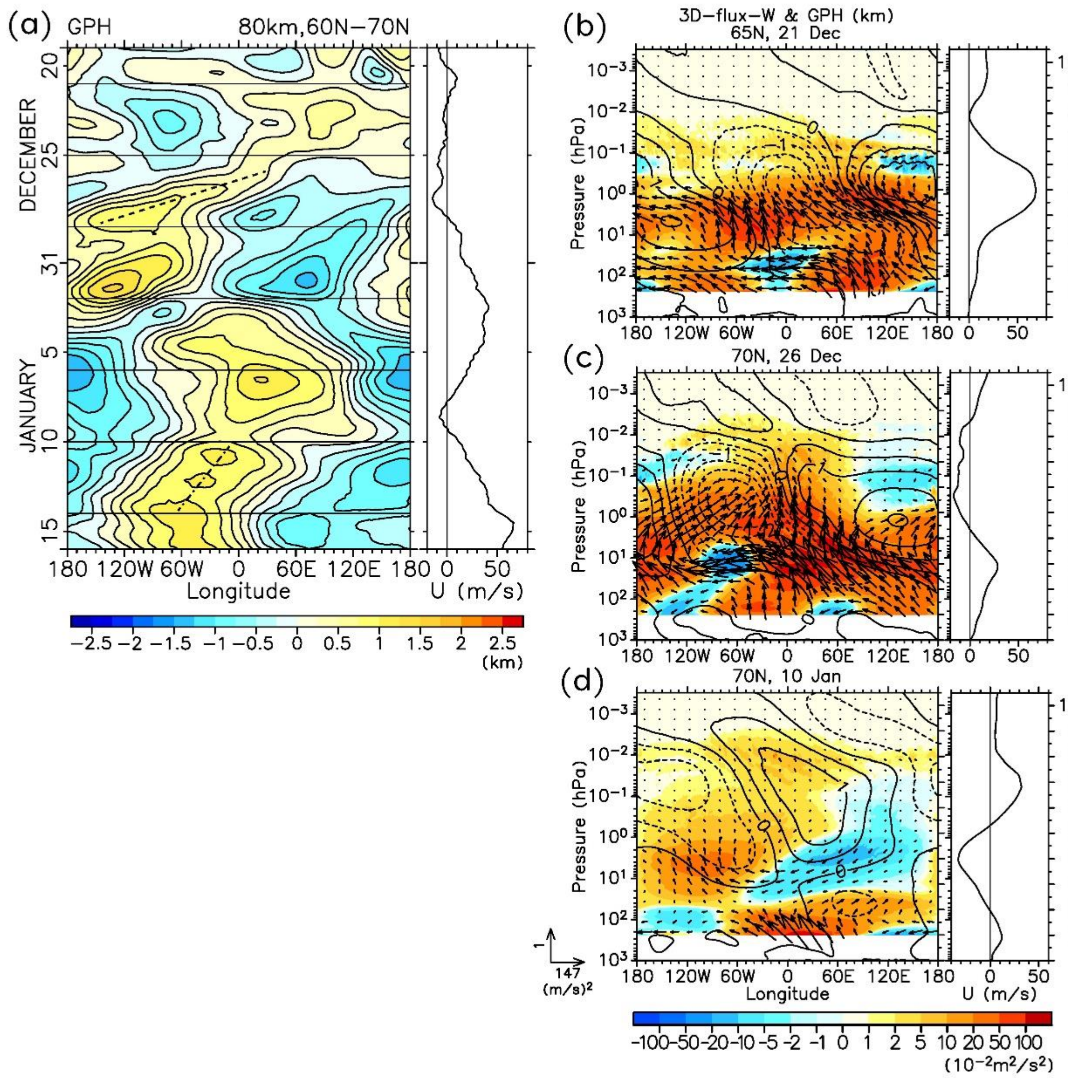

Figure 10. (a) Left panel: longitude–time section at 60° N–70° N, z= 80 km. Thin horizontal lines represent the boundaries of the model runs. A dashed line and a dash-dotted line denote propagations with periods of 6 days and 24 days, respectively; (b–d) left panel: latitude–height sections of geopotential height deviation from zonal mean (contours), vertical component of 3D-flux-W $\mathbf{F}_{w1}$ weighted by $\rho_0^{1/2}$ (shading) and the vertical and zonal components of 3D-flux-W $\mathbf{F}_{w1}$ weighted by $\rho_0^{1/2}$ (vectors) at (b) 65° N on 21 December 2018, (c) 70° N on 26 December 2018, and (d) 70° N on 10 January 2019; (a–d) right panels: variations with height of $[u]$ averaged over the same latitudinal region and time periods as the figures on the left.

3.4 Propagation of GWs

The GWs which play crucial roles in the formation of the ES and DS is further analyzed. Figure 11 shows the vertical flux of zonal momentum $[u^\dagger w^\dagger]$ of GWs as a function of the ground-based phase velocity c at each height. The solid and dashed curves denote the mean $[u]$ and $[u] \pm 1.65\sigma$ over a 20° latitude range centered around 50° N (Fig. 11a), 30° N (Fig. 11b), 60° N (Fig. 11c), and 60° N (Fig. 11d). Assuming normal distribution for $[u]$, the area between each pair of dashed curves encompasses 90% of the values of $[u]$. Figures 11a, 11b, 11c and 11d are the profiles for GWs at 50° N for 17–20 December (Case A), 30° N for 21–24 December (Case B), 60° N for 2–5 January (Case C) and 60° N for 10–13 January (Case D), respectively. As discussed in section 3.2, it is likely that in Cases A and B, GWs are responsible for the $[P_M]$ peaks that appear before the formation of the DS. The GW momentum flux in Case C is likely related to the reinforcement of the DS structure after SSW onset. In case D, GWs exert strong negative forcing in the MLT during the formation phase of the ES.

The vertical flux of zonal momentum $[u^\dagger w^\dagger]$ for Case A (Fig. 11a) is strongly negative around c= ~0 m s^{-1} at all altitudes. At its strongest, its absolute value exceeds ~0.1 m^2 s^{-2}. In Cases B, C and D, the negative $[u^\dagger w^\dagger]$ peaks around c= ~0 m s^{-1} in the troposphere and the lower stratosphere are absent in the upper stratosphere. This is likely because of weak wind layers in the lower or middle stratosphere.

In Case B, there is a weak wind layer with $[u]$= $\pm$10 m s^{-1} at z= 20–55 km; in addition to the small $[u]$, the variation of $[u]$, as indicated by the area between the two dashed lines is also small at z= 20–30 km. In Cases C and D, the weak wind layers of $[u]$= $\pm$10 m s^{-1} are at z= 25–50 km and z= 20–45 km, respectively. Because the meridional wind is generally weaker than $[u]$ and the meridional component of the ground-based phase velocity of a GW is smaller than the zonal component in most cases, GWs having c= ~0 m s^{-1} such as orographic waves break down at a critical layer, a layer with $[u]$= ~0 m s^{-1}. However, $[u^\dagger w^\dagger]$ of GWs having c= ~0 m s^{-1} above these layers are strongly negative at z= 65–100 km in Case B, z> 47 km in Case C and z> 55 km in Case D. The lowest values of $[u^\dagger w^\dagger]$ are ~-1×10^{-2} m^2 s^{-2} at z= 70–90 km in Case B, ~-1×10^{-2} m^2 s^{-2} at z= 75–95 km in Case C and ~-1×10^{-2} m^2 s^{-2} at z= 75–95 km in Case D. These negative momentum fluxes of GWs having c= ~0 m s^{-1} cannot be explained only by pure vertical propagation from the lower atmosphere, which is the assumption that is made in most GW parameterizations. This result indicates that these waves propagate from other latitudes and/or are excited in the middle atmosphere.

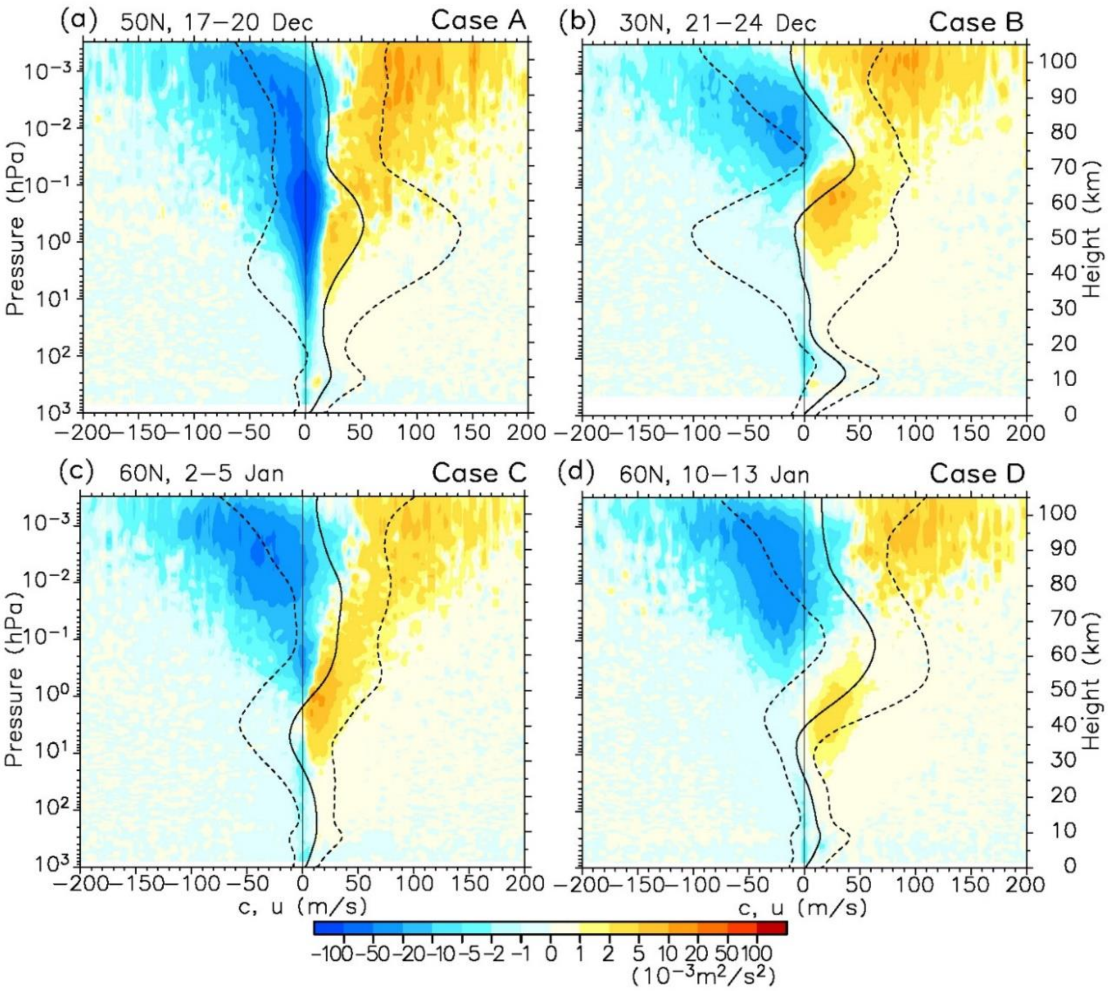

Figure 11. Vertical profiles of $[u^{\dagger}w^{\dagger}]$ of GWs as a function of the ground-based zonal phase velocity at each height (shading) at (a) 50° N for 17–20 December 2018 (Case A), (b) 30° N for 21–24 December 2018 (Case B), (c) 60° N for 2–5 January 2019 (Case C), and (d) 60° N for 10–13 January 2019 (Case D). The values $[u^{\dagger}w^{\dagger}]$ are smoothed by the 3-point moving average in the phase velocity direction. Solid curves denote the mean $[u]$ over a 20° latitude range centered around (a) 50° N, (b) 30° N, (c) 60° N, and (d) 60° N. Dashed curves on either side of the solid curve denote $[u]\pm1.65\sigma$, where σ is the standard deviation. Assuming normal distribution for $[u]$, the area between each pair of dashed curves encompasses 90% of the values of $[u]$.

4 Summary and Conclusions

To clarify the middle atmosphere dynamics in a significant SSW ES event in 2018/19, we performed a hindcast using a GW-permitting model that covers the ground surface to the lower thermosphere. Detailed analysis of the output data indicates crucial importance of the interplay between PWs and GWs.

We have first reported a double stratopause (DS) structure: A temperature maximum was located at a height of z= ~85 km in the polar region before the disappearance of the lowered stratopause associated with an SSW (Figs. 1a and 1b). Thus, there are two temperature maxima in the vertical profile during the time period.

To examine the mechanism of the formation of the DS, a schematic of the mechanism is shown in Fig. 12. Prior to DS formation, during 17–20 December, GWF above the eastward polar night jet was strongly negative at ~50° N, z= ~65 km (Fig. 3a); GWF was positive above the westward wind at <35° N and z= ~65 km, equatorward of the negative GWF. Because of the residual mean upward flow induced below, the residual mean vertical flow converged in the region between the negative and positive GWFs (Fig. 4a). A peak of P_M appeared as a result of N^2 increase in this region of convergence, which was located at ~40° N, θ= ~3,500 K (z= ~65 km).

During 21–24 December, PWF was positive poleward of the $[P_M]$ peak that was present in 17–20 December (Fig. 3b). This feature suggests the in-situ generation of PWs due to the BT/BC instability. During this period, negative (positive) GWF appeared above (below) the eastward jet with its axis at ~25° N and z= ~72 km in the mesosphere. This GWF distribution can be explained by a filtering effect by the mesospheric eastward jet. This jet tilted from the equatorial region in the lower mesosphere to the winter polar region in the upper mesosphere. A weak temperature maximum extending toward higher altitudes and latitudes was formed at the height of residual mean downwelling, which was located between the negative and positive GWFs in the mesosphere. There was also a residual mean upward flow poleward of the positive GWF. Then, a $[P_M]$ peak caused by high N^2 appeared in the region where the vertical flow converged (Fig. 4b). Poleward of this peak, $[P_M]_y$ was negative, which satisfied the necessary condition of the BT/BC instability.

During 25–28 December, PWF was positive where $[P_M]_y$< 0 in 21–24 December (Fig. 3c). It is also likely that PWs were generated due to the BT/BC instability induced by the GWFs in the mesosphere. In addition, PWF in the MLT was strongly negative. This negative PWF was probably a result of the PWs generated in the mesosphere because the prevailing wind was westward in the stratosphere during the major SSW, and PWs excited in the troposphere hardly propagate through into the MLT. It is inferred that a downward flow induced by the negative PWF in the polar MLT caused the upper maximum of the DS at z= ~85 km.

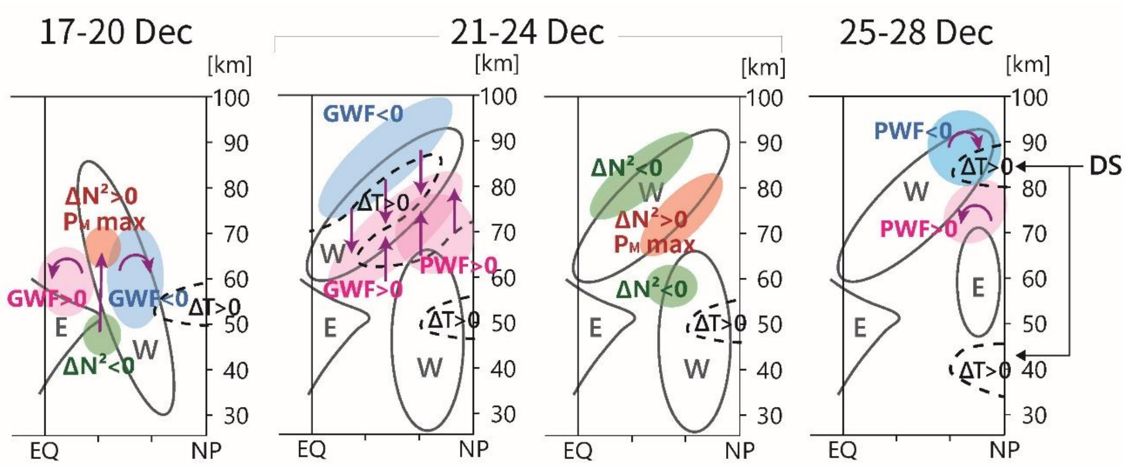

Figure 12. A schematic of the formation mechanism of the DS in the latitude–height section; W and E denote westerly (eastward) and easterly (westward) winds; Δ represents the anomaly of each value; purple vectors indicate the residual mean flows.

To examine the mechanism of the formation of the ES, a schematic of the mechanism is shown in Fig. 13. During 2–5 January, after the onset of major warming on 1 January, the DS structure was reinforced by the negative GWF in the polar MLT (Figs. 2d and 5a). Then, PWF was negative throughout the entire polar middle atmosphere during 6–9 January (Figs. 2b and 5b). As a result, the westward wind in the polar mesosphere, which had disappeared in 2–5 January, was reformed at z< 90 km in 6–9 January. Then, a $[P_M]$ maximum appeared at ~60° N and θ= 3,000–6,000 K (z= 60–80 km) (Fig. 5b). The orthographic projection map of θ= 4,000 K (z= ~70 km) shows high P_M inside of a comma-like polar vortex, which is a typical feature of PW breaking (Fig. 7a).

During 10–13 January, PWF was positive poleward of 60° N at z= 35–80 km (Fig. 5c), in a region that roughly matches the region of $[P_M]_y$< 0 in 6–9 January. These features suggest that PWs were generated in-situ by the BT/BC instability. During 10–13 January, GWF and PWF were negative at z> 80 km above the recovered eastward jet in the polar mesosphere (Fig. 5c, also Figs. 2b and 2d). These wave forcings were comparable in strength and had values of -20 to -50 m s^{-1} d^{-1} in the polar MLT. The ES was formed at z= ~80 km around 11 January (Fig. 5c, also Figs. 1a and 1b). The PWF appeared above the prevailing westward wind in the stratosphere. Thus, this forcing may be from PWs generated at >60° N, z= 35–80 km on 10 January. These results indicate that both GWF and PWF played significant roles in the formation of the ES. Observed longitudinal structure of the polar temperature suggests that the zonally asymmetric ES was a warming inside of the polar vortex (Fig. 8). The structure of the ES was likely to be determined by the zonally asymmetric GWF and PWF (Fig. 9).

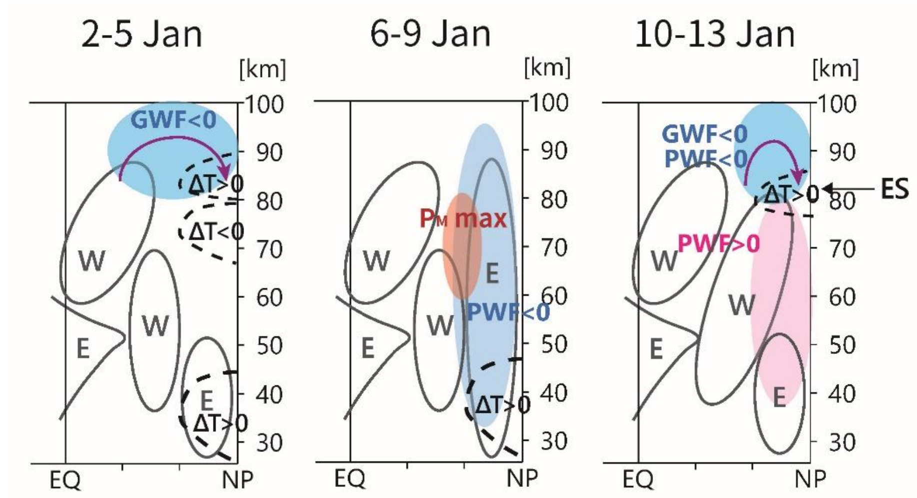

Figure 13. A schematic of the formation mechanism of the ES in the latitude–height section. Symbols are the same as those in Fig. 12.

Our results also suggest that the DS structure may have affected the process of ES formation. The reformation of the mesospheric westward wind during 6–9 January prevented upward PW propagation. Without adiabatic heating associated with wave forcing, the latitudinal gradient of zonal mean temperature $[T]_y$ tends to decline gradually because of radiative relaxation in the polar night region. The height dependency of $[T]_y$ may be affected by the temperature structure as a result of the DS, as shown in Fig. 13 for the first period of 2–5 January. The DS structure had a $[T]$ minimum at z= 65–77 km and a maximum at z= 80–90 km. At the altitudes where the $[T]$ minimum was present, $[T]_y$ became strongly negative. The altitude of the recovered eastward jet was determined by $[T]_y$ via the thermal wind balance. Thus, the height of the eastward jet was probably modified by the DS structure. The eastward jet affected the propagation of GWs and PWs and their forcings in the polar MLT, leading to the formation of the ES. In this way, it is likely that the height of the ES was affected by the DS structure.

From the relationship between phase velocity spectra of GW momentum fluxes and the vertical profile of zonal-mean zonal wind, it is shown that vertical propagation from the lower atmosphere alone is insufficient to explain the presence of the GWs, which play important roles in the formation of the DS and ES (Fig. 11). It is suggested that a part of these GWs propagated laterally and/or were generated in the middle atmosphere. This result indicates that the assumptions generally underlying GW parameterizations are not necessarily appropriate for representing GWs in the MLT.

Results from the high-resolution JAGUAR are generally consistent with observations and enable quantitative analysis of the middle atmosphere dynamics including GWs. Although this study focused on the dynamics in the Northern Hemisphere, JAGUAR provides promising data that can be used to examine the mechanisms of various dynamical phenomena observed in the entire middle atmosphere, such as interhemispheric coupling (e.g., Körnich and Becker, 2010).

Acknowledgments

All figures in this paper were created using Dennou Club Library (DCL). This study benefitted from stimulating discussions at the International Space Science Institute (ISSI) Gravity Wave activity. The author (HO) is grateful to T. Kinoshita, M. Kohma and S. Noguchi for fruitful discussions. The study was supported by JST CREST (grant JPMJCR1663). The hindcasts were performed using the Earth Simulator at the Japan Agency for Marine-Earth Science and Technology (JAMSTEC). The processed model data are available at the following website: http://pansy.eps.s.u-tokyo.ac.jp/en/archive_data/Okui_etal_2021/. The Aura MLS observation data can be obtained from the NASA Goddard Space Flight Center Earth Science Data and Information Services Center (GES-DISC, https://disc.gsfc.nasa.gov/). English of a draft of this manuscript was grammatically edited by T. Tin from Edanz Group (https://en-author-services.edanz.com/ac).

References

Andrews, D. G., & McIntyre, M. E. (1976). Planetary Waves in Horizontal and Vertical Shear: The Generalized Eliassen-Palm Relation and the Mean Zonal Acceleration. *Journal of the Atmospheric Sciences*, **33**, 2031–2048, https://doi.org/10.1175/1520-0469(1976)033<2031:PWIHAV>2.0.CO;2

Baldwin, M., & Holton, J. (1988). Climatology of the stratospheric polar vortex and planetary wave breaking. *Journal of the Atmospheric Sciences*, **45**, 1123–1142, https://doi.org/10.1175/1520-0469(1988)045,1123:COTSPV.2.0.CO;2

Bloom, S. C., Takacs, L. L., DaSilva, A. M., & Levina, D. (1996). Data assimilation using incremental analysis updates. *Monthly Weather Review*, **124**, 1256–1271. https://www.researchgate.net/deref/http%3A%2F%2Fdx.doi.org%2F10.1175%2F1520-0493(1996)124%3C1256%3ADAUIAU%3E2.0.CO%3B2

Chandran, A., Collins, R. L., Garcia, R. R., & Marsh, D. R. (2011). A case study of an elevated stratopause generated in the Whole Atmosphere Community Climate Model. *Geophysical Research Letters*, **38**, L08804. https://doi.org/10.1029/2010GL046566

Chandran, A., Collins, R. L., Garcia, R. R., Marsh, D. R., Harvey, V. L., Yue, J., & De La Torre, L. (2013). A climatology of elevated stratopause events in the whole atmosphere community climate model. *Journal of Geophysical Research: Atmospheres*, **118**, 1234–1246. https://doi.org/10.1002/jgrd.50123

Chandran, A., Collins, R. L., & Harvey, V. L. (2014). Stratosphere-mesosphere coupling during stratospheric sudden warming events. *Advances in Space Research*, **53**, 1265–1289. https://doi.org/10.1016/j.asr.2014.02.005

Charlton, A. J., & Polvani, L. M. (2007). A New Look at Stratospheric Sudden Warmings. Part I: Climatology and Modeling Benchmarks. *Journal of Climate*, **20**, 449–469, https://doi.org/10.1175/JCLI3996.1

Charney, J. G., & Drazin, P. G. (1961). Propagation of planetary‐scale disturbances from the lower into the upper atmosphere. *Journal of Geophysical Research*, **66**(1), 83−109. https://doi.org/10.1029/jz066i001p00083

Ern, M., Trinh, Q. T., Preusse, P., Gille, J. C., Mlynczak, M. G., Iii, J. M. R., & Riese, M. (2018). GRACILE: A comprehensive climatology of atmospheric gravity wave parameters based on satellite limb soundings. *Earth System Science Data*, **10**, 857–892. https://doi.org/10.5194/essd−10-857-2018

France, J. A., & Harvey, V. L. (2013). A climatology of the stratopause in WACCM and the zonally asymmetric elevated stratopause. *Journal of Geophysical Research: Atmospheres*, **118**, 2241–2254. https://doi.org/10.1002/jgrd.50218

Funke, B., Ball, W., Bender, S., Gardini, A., Harvey, V. L., Lambert, et al. (2017). HEPPA-II model-measurement intercomparison project: EPP indirect effects during the dynamically perturbed NH winter 2008-2009. *Atmospheric Chemistry and Physics*, **17**, 3573–3604. https://doi.org/10.5194/acp−17-3573-2017

Greer, K., Thayer, J. P., & Harvey, V. L. (2013). Aclimatology of polar winter stratopause warmings and associated planetary wave breaking. *Journal of Geophysical Research: Atmospheres*, **118**, 4168–4180, https://doi.org/10.1002/jgrd.50289

Harada, Y., Sato, K., Kinoshita, T., Yasui, R., Hirooka, T., & Naoe, H. (2019). Diagnostics of a WN2-Type Major Sudden Stratospheric Warming Event in February 2018 Using a New Three-Dimensional Wave Activity Flux. *Journal of Geophysical Research: Atmospheres*, **124**, 6120–6142. https://doi.org/10.1029/2018JD030162

Hitchman, M. H., & Huesmann, A. S. (2007). A Seasonal Climatology of Rossby Wave Breaking in the 320–2000-K Layer. *Journal of the Atmospheric Sciences*, **64**, 1922–1940, https://doi.org/10.1175/JAS3927.1

Holt, L. A., Randall, C. E., Peck, E. D., Marsh, D. R., Smith, A. K., & Harvey, V. L. (2013). The influence of major sudden stratospheric warming and elevated stratopause events on the effects of energetic particle precipitation in WACCM. *Journal of Geophysical Research: Atmospheres*, **118**, 11,636−11,646. https://doi.org/10.1002/2013JD020294

Kinoshita, T., & Sato, K. (2013). A formulation of unified three-dimensional wave activity flux of inertia-gravity waves and Rossby waves. *Journal of the Atmospheric Sciences*, **70**, 1603–1615. https://doi.org/10.1175/JAS-D−12-0138.1

Kinoshita, T., Sato, K., Ishijima, K., Takigawa, M., & Yamashita, Y. (2019). Formulation of three-dimensional quasi-residual mean flow balanced with diabatic heating rate and potential vorticity flux. *Journal of the Atmospheric Sciences.*, **76**, 851–863. https://doi.org/10.1175/JAS-D−18-0085.1

Körnich, H., & Becker, E. (2010). A simple model for the interhemispheric coupling of the middle atmosphere circulation. *Advances in Space Research*, **45**, 661–668. https://doi.org/10.1016/j.asr.2009.11.001

Koshin, D., Sato, K., Miyazaki, K., & Watanabe, S. (2020). An ensemble Kalman filter data assimilation system for the whole neutral atmosphere. *Geoscientific Model Development*, **13**, 3145–3177, https://doi.org/10.5194/gmd−13-3145-2020

Lait, L. R. (1994). An alternative form for potential vorticity. *Journal of the Atmospheric Sciences*, **51**, 1754–1759. https://doi.org/10.1175/1520-0469(1994)051<1754:AAFFPV>2.0.CO;2

Limpasuvan, V., Orsolini, Y. J., Chandran, A., Garcia, R. R., & Smith, A. K. (2016). On the composite response of the MLT to major sudden stratospheric warming events with elevated stratopause. *Journal of Geophysical Research: Atmospheres*, **121**,4518–4537, https://doi.org/10.1002/2015JD024401

Limpasuvan, V., Richter, J. H., Orsolini, Y. J., Stordal, F., & Kvissel, O. K. (2012). The roles of planetary and gravity waves during a major stratospheric sudden warming as characterized in WACCM. *Journal of Atmospheric and Solar-Terrestrial Physics*, **78–79**, 84–98. https://doi.org/10.1016/j.jastp.2011.03.004

Manney, G. L., Krüger, K., Pawson, S., Minschwaner, K., Schwartz, M. J., Daffer, W. H., et al. (2008). The evolution of the stratopause during the 2006 major warming: Satellite data and assimilated meteorological analyses. *Journal of Geophysical Research*, **113**, D11115. https://doi.org/10.1029/2007jd009097

Manney, G. L., Schwartz, M. J., Krüger, K., Santee, M. L., Pawson, S., Lee, J. N., Daffer, W. H., Fuller, R. A., & Livesey, N. J. (2009). Aura Microwave Limb Sounder observations of dynamics and transport during the record-breaking 2009 Arctic stratospheric major warming. *Geophysical Research Letters*, **36**, L12815. https://doi.org/10.1029/2009GL038586

Matsuno, T. (1971). A Dynamical Model of the Stratospheric Sudden Warming. *Journal of the Atmospheric Sciences.*, **28**, 1479–1494. https://doi.org/10.1175/1520-0469(1971)028<1479:ADMOTS>2.0.CO;2

Meraner, K., Schmidt, H., Manzini, E., Funke, B., & Gardini, A. (2016). Sensitivity of simulated mesospheric transport of nitrogen oxides to parameterized gravity waves. *Journal of Geophysical Research: Atmospheres*, **121**, 12,045–12,061. https://doi.org/10.1002/2016JD025012

Orsolini, Y. J., Limpasuvan, V., Pérot, K., Espy, P., Hibbins, R., Lossow, S., et al. (2017). Modelling the descent of nitric oxide during the elevated stratopause event of January 2013. *Journal of Atmospheric and Solar-Terrestrial Physics*, **155**, 50–61. https://doi.org/10.1016/j.jastp.2017.01.006

Randall, C. E., Harvey, V. L., Siskind, D. E., France, J., Bernath, P. F., Boone, C. D., & Walker, K. A. (2009). NOx descent in the arctic middle atmosphere in early 2009. *Geophysical Research Letters*, **36**, 2007–2010. https://doi.org/10.1029/2009GL039706

Sato, K., Kohma, M., Tsutsumi, M., & Sato, T. (2017). Frequency spectra and vertical profiles of wind fluctuations in the summer Antarctic mesosphere revealed by MST radar observations, *Journal of Geophysical Research: Atmospheres*, **122**, 3-19. https://doi.org/10.1002/2016JD025834

Sato, K., & Nomoto, M. (2015). Gravity wave-induced anomalous potential vorticity gradient generating planetary waves in the winter mesosphere. *Journal of the Atmospheric Sciences*, **72**, 3609–3624. https://doi.org/10.1175/JAS-D−15-0046.1

Sato, K., Tateno, S., Watanabe, S., & Kawatani, Y. (2012). Gravity Wave Characteristics in the Southern Hemisphere Revealed by a High-Resolution Middle-Atmosphere General Circulation Model. *Journal of the Atmospheric Sciences*, **69**, 1378–1396, https://doi.org/10.1175/JAS-D−11-0101.1

Sato, K., Watanabe, S., Kawatani, Y., Tomikawa, Y., Miyazaki, K., & Takahashi, M. (2009). On the origins of gravity waves in the mesosphere. *Geophysical Research Letters*, **36**, L19801, https://doi.org/10.1029/2009GL039908

Sato, K., R. Yasui, & Y. Miyoshi (2018). The momentum budget in the stratosphere, mesosphere, and lower thermosphere. Part I: contributions of different wave types and in situ generation of Rossby waves. *Journal of the Atmospheric Sciences*, **75**, 3613–3633, https://doi.org/10.1175/JAS-D−17-0336.1

Shibuya, R., & Sato, K. (2019). A study of the dynamical characteristics of inertia-gravity waves in the Antarctic mesosphere combining the PANSY radar and a non-hydrostatic general circulation model. *Atmospheric Chemistry and Physics*, **19**, 3395–3415. https://doi.org/10.5194/acp−19-3395-2019

Shibuya, R., Sato, K., Tsutsumi, M., Sato, T., Tomikawa, Y., Nishimura, K., & Kohma, M. (2017). Quasi−12 h inertia-gravity waves in the lower mesosphere observed by the PANSY radar at Syowa Station (39.6° E, 69.0° S). *Atmospheric Chemistry and Physics*, **17**, 6455–6476. https://doi.org/10.5194/acp−17-6455-2017

Siskind, D. E., Eckermann, S. D., Coy, L., McCormack, J. P., & Randall, C. E. (2007). On recent interannual variability of the Arctic winter mesosphere: Implications for tracer descent. *Geophysical Research Letters*, **34**, L09806. https://doi.org/10.1029/2007GL029293

Siskind, D. E., Eckermann, S. D., McCormack, J. P., Coy, L., Hoppel, K. W., & Baker, N. L. (2010). Case studies of the mesospheric response to recent minor, major, and extended stratospheric warmings. *Journal of Geophysical Research: Atmospheres*, **115**, D00N03. https://doi.org/10.1029/2010JD014114

Siskind, D. E., Sassi, F., Randall, C. E., Harvey, V. L., Hervig, M. E., & Bailey, S. M. (2015). Is a high-altitude meteorological analysis necessary to simulate thermosphere-stratosphere coupling? *Geophysical Research Letters*, **42**, 8225–8230. https://doi.org/10.1002/2015GL065838

Smith, A. K. (1996). Longitudinal Variations in Mesospheric Winds: Evidence for Gravity Wave Filtering by Planetary Waves. *Journal of the Atmospheric Sciences*, **53**, 1156–1173, https://doi.org/10.1175/1520-0469(1996)053<1156:LVIMWE>2.0.CO;2

Smith, A. K. (2003). The Origin of Stationary Planetary Waves in the Upper Mesosphere. *Journal of the Atmospheric Sciences*, **60**, 3033–3041. https://doi.org/10.1175/1520-0469(2003)060<3033:TOOSPW>2.0.CO;2

Smith, A. K., Espy, P. J., López-Puertas, M., & Tweedy, O. V. (2018). Spatial and Temporal Structure of the Tertiary Ozone Maximum in the Polar Winter Mesosphere. *Journal of Geophysical Research: Atmospheres*, **123**, 4373–4389. https://doi.org/10.1029/2017JD028030

Stray, N. H., Orsolini, Y. J., Espy, P. J., Limpasuvan, V., & Hibbins, R. E. (2015). Observations of planetary waves in the mesosphere-lower thermosphere during stratospheric warming events. *Atmospheric Chemistry and Physics*, **15**, 4997–5005. https://doi.org/10.5194/acp−15-4997-2015

Thurairajah, B., Bailey, S. M., Cullens, C. Y., Hervig, M. E., & Russell III, J. M. (2014). Gravity wave activity during recent stratospheric sudden warming events from SOFIE temperature measurements. *Journal of Geophysical Research: Atmospheres*, **119**, 8091–8103, https://doi.org/10.1002/2014JD021763

Tomikawa, Y., Sato, K., Watanabe, S., Kawatani, Y., Miyazaki, K., & Takahashi, M. (2012). Growth of planetary waves and the formation of an elevated stratopause after a major stratospheric sudden warming in a T213L256 GCM. *Journal of Geophysical Research: Atmospheres*, **117**, D16101. https://doi.org/10.1029/2011JD017243

Vadas, S. L., & Becker, E. (2018). Numerical modeling of the excitation, propagation, and dissipation of primary and secondary gravity waves during wintertime at McMurdo Station in the Antarctic. *Journal of Geophysical Research: Atmospheres*, **123**, 9326–9369. https://doi.org/10.1029/2017JD027974

Watanabe, S., Kawatani, Y., Tomikawa, Y., Miyazaki, K., Takahashi, M., & Sato, K. (2008). General aspects of a T213L256 middle atmosphere general circulation model. *Journal of Geophysical Research: Atmospheres*, **113**, D12110. https://doi.org/10.1029/2008JD010026

Watanabe, S., & Miyahara, S. (2009). Quantification of the gravity wave forcing of the migrating diurnal tide in a gravity wave-resolving general circulation model. *Journal of Geophysical Research: Atmospheres*, **114**, D07110. https://doi.org/10.1029/2008JD011218

Watanabe, S., Tomikawa, Y., Sato, K., Kawatani, Y., Miyazaki, K., & Takahashi, M. (2009). Simulation of the eastward 4-day wave in the Antarctic winter mesosphere using a gravity wave resolving general circulation model. *Journal of Geophysical Research: Atmospheres*, **114**, D16111. https://doi.org/10.1029/2008JD011636

Yamashita, C., England, S. L., Immel, T. J., & Chang, L. C. (2013). Gravity wave variations during elevated stratopause events using SABER observations. *Journal of Geophysical Research: Atmospheres*, **118**, 5287–5303. https://doi.org/10.1002/jgrd.50474

Yasui, R., K. Sato, & Y. Miyoshi. (2018). The momentum budget in the stratosphere, mesosphere, and lower thermosphere. Part II: The in situ generation of gravity waves. *Journal of the Atmospheric Sciences*, **75**, 3635–3651. https://doi.org/10.1175/JAS-D−17-0337.1